Atlantic Equatorial Undercurrent and associated cold tongue variability

Verena Hormann[1] and Peter Brandt[1]

[1]   The Atlantic Equatorial Undercurrent (EUC) is studied using a simulation for the period 1990–2002 with a high-resolution ocean general circulation model. Simulated transports of the EUC that supplies the annual mean upwelling in the central and eastern equatorial Atlantic are in good agreement with new transport estimates derived from ship observations, i.e., 19.9 and 14.0 Sv at 35°W and 23°W, respectively. Although the observations are not conclusive concerning the seasonal cycle of EUC transports, the simulated seasonal cycles fit largely in the observed range. The analysis of the EUC variability associated with interannual boreal summer variability of the equatorial cold tongue showed that cold tongue indices, defined either by near-surface temperature or steric height anomalies, are anticorrelated with thermocline EUC transport anomalies: A strong EUC corresponds to low near-surface temperatures and steric heights. The importance of equatorial waves for the cold tongue region is shown: Surface layer transport anomalies at 23°W and 10°W are significantly correlated with both near-surface temperature and steric height anomalies in the equatorial and coastal upwelling regions, indicating an associated eastward phase propagation along the equator toward the African coast where the signal bifurcates into two poleward branches along the coast and is reflected into a westward propagating wave.

1.   Introduction

[2]   The eastern tropical Atlantic, with its characteristic cold tongue, is a region where upper ocean variability appears in the most obvious way through sea surface temperature (SST) anomalies. During boreal summer, SST anomalies along the equator and to the south in the eastern equatorial cold tongue region are well correlated with rainfall variability over the tropical ocean and adjacent land regions, in particular, northeast Brazil and coastal regions surrounding the Gulf of Guinea [e.g., *Giannini et al.*, 2003; *Xie and Carton*, 2004; *Kushnir et al.*, 2006; *Chang et al.*, 2006]. Thus this correlation suggests a potential predictability of rainfall variability in case of a predictability of SST. In this context, oceanic processes are of significance, particularly horizontal advection via the zonal currents supplying the eastern upwelling regions [*Foltz et al.*, 2003; *Yu et al.*, 2006]. The Atlantic subtropical cells (STCs) connect the subtropical subduction regions of both hemispheres to the eastern equatorial upwelling regimes by equatorward thermocline and poleward surface flows [e.g., *Liu et al.*, 1994; *McCreary and Lu*, 1994; *Malanotte-Rizzoli et al.*, 2000]. One function of the STCs is to provide the cool subsurface water that is required to maintain the

tropical thermocline. For this reason, STC variability has been hypothesized to be important for the decadal modulation of El Niño Southern Oscillation (ENSO) and for Pacific decadal variability, and it may affect Atlantic equatorial SST as well [*Snowden and Molinari*, 2003; *Schott et al.*, 2004]. In the Atlantic, STC pathways are complicated by their interaction with the other ocean currents, in particular, the northward flow of warm water by the Meridional Overturning Circulation (MOC [*Ganachaud and Wunsch*, 2001; *Lumpkin and Speer*, 2003]). As a consequence of these interactions, the southern STC is stronger than the northern one [e.g., *Malanotte-Rizzoli et al.*, 2000; *Fratantoni et al.*, 2000; *Zhang et al.*, 2003]. The STCs also interact with even shallower overturning cells confined to the tropics that are associated with downwelling driven by the decrease of the poleward Ekman transport 4–6° off the equator [e.g., *Liu et al.*, 1994; *McCreary and Lu*, 1994]. *Inui et al.* [2002] pointed out that the Atlantic STCs are sensitive to changes in wind stress, and it has been established that wind-driven STC transport variations ($v'\bar{T}$ hypothesis: *Kleeman et al.* [1999]) are more relevant than advection of subducted temperature anomalies by the mean STC currents ($\bar{v}T'$ hypothesis: *Gu and Philander* [1997]) in generating equatorial SST anomalies [*Schott et al.*, 2004]. The Equatorial Undercurrent (EUC) is the primary equatorial branch of the STCs and seems to terminate near the eastern boundary [*Schott et al.*, 2004]. In the western source region, the Atlantic EUC is predominantly supplied from the Southern Hemisphere as a consequence of the northward flowing upper branch of the

---

[1]Leibniz-Institut für Meereswissenschaften an der Universität Kiel, Kiel, Germany.

MOC [e.g., *Fratantoni et al.*, 2000; *Schott et al.*, 2002; *Hazeleger et al.*, 2003]. Studying the fate of the Atlantic EUC, *Hazeleger and de Vries* [2003] showed that most EUC water upwells in the equatorial region. Thus understanding EUC variability is important because it can affect SST through its effects on equatorial upwelling.

[3] The seasonal cycle of the Atlantic EUC, with focus on the western and central parts of the basin, has been addressed by a variety of model studies, and there is general agreement that the transport cycle can be characterized by two maxima: the primary one during boreal summer/autumn and another during boreal winter/spring [*Philander and Pacanowski*, 1986b; *Schott and Böning*, 1991; *Hazeleger et al.*, 2003; *Arhan et al.*, 2006; *Hüttl and Böning*, 2006].

[4] Presently, little can be said about the seasonal cycle of EUC transport from observations, but a sufficient number of cross-equatorial ship sections are now available at 35°W and near 23°W to afford reasonable estimates of the mean EUC structure and transport at these locations [*Schott et al.*, 2003; *Brandt et al.*, 2006]. Farther east, measurements are sparse, and the observed snapshot transports indicate a large variability of the current system [*Hisard and Hénin*, 1987; *Bourlès et al.*, 2002; *Mercier et al.*, 2003].

[5] In the Pacific, mean transport and seasonal cycle of the EUC are fairly well known across most of the basin, and EUC variability is known to occur in association with SST variations in the eastern cold tongue region on both seasonal and interannual timescales [*Philander et al.*, 1987; *Yu and McPhaden*, 1999; *Keenlyside and Kleeman*, 2002; *Johnson et al.*, 2002; *Izumo*, 2005]. The key element responsible for the development of Pacific ENSO events is the dynamical feedback mechanism described by *Bjerknes* [1969]. Like the ENSO mode, the underlying feedback of warm (cold) episodes in the equatorial Atlantic cold tongue region during boreal summer is also thought to be the dynamical Bjerknes mechanism [e.g., *Zebiak*, 1993; *Xie and Carton*, 2004; *Chang et al.*, 2006; *Keenlyside and Latif*, 2007], but observations are more limited. In this study, we therefore use a high-resolution ocean model to investigate the Atlantic EUC and associated cold tongue variability.

[6] The remainder of this paper is organized as follows. Section 2 provides a description and extensive validation of the used model. Mean and seasonal cycle in the central and eastern equatorial Atlantic are addressed in section 3, whereas section 4 deals with the interannual variability. Finally, the results are summarized and discussed in section 5.

2. Models and Data

2.1. FLAME

[7] This study is based on monthly mean fields of a numerical model simulation performed as part of the Family of Linked Atlantic Ocean Model Experiments (FLAME) hierarchy of models for studying various aspects of the Atlantic Ocean [*Dengg et al.*, 1999]. FLAME follows up the kind of ocean models as used in the Community Modeling Effort (CME [*Bryan and Holland*, 1989; *Böning and Bryan*, 1996]) and the European Dynamics of North Atlantic Models (DYNAMO) ocean model intercomparison study [*Willebrand et al.*, 2001]. The numerical code (http://www.ifm-geomar.de/~spflame) is based on a refined configuration [*Redler et al.*, 1998] of the GFDL MOM

2.1 code [*Pacanowski*, 1995]. The model domain covers the Atlantic Ocean between 18°S and 70°N, 100°W and 30°E, with a horizontal resolution of 1/12° in longitude and 1/12° cos ϕ in latitude. This z-coordinate model version uses 45 levels in the vertical, with 10-m resolution near the surface, smoothly increasing to a maximum of 250 m below 2250 m. Vertical mixing is parameterized based on the stability-dependent scheme for vertical diffusivity ($\kappa_h = 0.1$–4.0 cm^2/s) and viscosity ($\kappa_m = 2.0$–10.0 cm^2/s) as described in the study by *Böning and Kröger* [2005], and a KT scheme [*Kraus and Turner*, 1967] is used for the mixed layer. The model uses biharmonic friction and isopycnal diffusion, with a diffusivity of 50 m^2/s and a viscosity of 2×10^{10} m^4/s. The model spin-up starts from the Levitus climatology [*Boyer and Levitus*, 1997] for 10 model years under climatological forcing, based on the monthly mean wind stresses and linearized heat fluxes as derived from European Center for Medium-Range Weather Forecast (ECMWF) analyses for the years 1986–1988 by *Barnier et al.* [1995]. The surface heat flux includes a relaxation to climatological SST in a formulation following the work of *Haney* [1971]:

$$Q = Q_0 + Q_2(\text{SST}_{\text{model}} - \text{SST}_{\text{clim}}) \tag{1}$$

with $Q_2 = \frac{\partial Q}{\partial \text{SST}}|_{\text{SST}_{\text{clim}}}$ and Q_0 denotes the prescribed surface heat flux. The spin-up phase is followed by an interannually forced period from 1987 to 2003, based on the National Center for Environmental Prediction/National Center for Atmospheric Research (NCEP/NCAR) reanalysis [*Kalnay et al.*, 1996]; that is, the variable surface forcing is realized by adding the monthly net heat flux and wind stress anomalies from the NCEP/NCAR reanalysis to the ECMWF-based climatology data. In the present study, monthly output fields of the time period from 1990 to 2002 are used. Further details and specifications are found in the works of, e.g., *Eden and Böning* [2002] and *Hüttl and Böning* [2006].

[8] Monthly mean output fields of the last two spin-up years of a second experiment (SPFLAME), based on the same numerical code and with the same vertical and horizontal resolution as described above, are also used. Subgrid-scale parameterizations are here biharmonic friction and diffusion (with diffusivity of 0.8×10^{10} m^4/s and viscosity of 2×10^{10} m^4/s) and a closure for the vertical turbulent kinetic energy (TKE) following the study by *Gaspar et al.* [1990]. The surface forcing is due to the monthly fields of the ECMWF climatology which were linearly interpolated onto the model time. For further information, see, e.g., *Eden* [2006].

2.2. Data

[9] Additionally, 16 cross-equatorial ship sections at 35°W are used in this study as well as 13 sections carried out between 29°W and 23°W. Updated mean sections of zonal currents at 35°W [*Schott et al.*, 2003] and near 23°W [*Brandt et al.*, 2006] are derived, now including the Meteor cruises of May (~23°W between 2°S and 0.5°N) and June/July 2006 (35°W between 5°S and 5°N; 23°W between 4°S and 5°N). As described by *Brandt et al.* [2006], above 30 m, the mean flow fields are linearly interpolated toward the mean surface flow obtained from the surface drifter climatology by *Lumpkin and Garzoli* [2005].

[10] The surface drifter climatology by *Lumpkin and Garzoli* [2005] is also used for comparison with the model's surface velocities. Monthly mean fields of the tropical Atlantic, available on a regular $1° \times 1°$ grid, were derived by combining and integrating time-mean, annual, and semiannual components of the total velocity. Results were smoothed via optimum interpolation (OI), assuming a Gaussian autocorrelation function with an isotropic e-folding scale of 150 km.

[11] Furthermore, two different SST products are used in this study: National Oceanic and Atmospheric Administration (NOAA) and Microwave (MW; http://www.remss.com) OI data sets. The NOAA OI SST monthly fields (version 2) were derived by a linear interpolation of the corresponding weekly OI fields to daily fields and then averaging the daily values over a month [*Reynolds et al.*, 2002]. The horizontal resolution is globally $1° \times 1°$, and monthly averages are available from November 1981 onward. Besides, the daily MW OI SST data set based on the microwave imager on board the Tropical Rainfall Measuring Mission (TRMM) satellite covers the oceans between $±40°$ in latitude for the period January 1998 to present. SSTs were blended together using the OI scheme described by *Reynolds and Smith* [1994], with a horizontal resolution of $0.25° \times 0.25°$.

[12] We also use the along-track Topex/Poseidon (T/P) sea surface anomaly (SSA) data set produced by the Jet Propulsion Laboratory, Physical Oceanography Distributed Active Archive Center (PO.DAAC). This data set is organized as 10-day repeat cycles and available from September 1992 onward. The SSA represents the difference between the best estimate of the sea surface height and a mean sea surface. The sea surface height was corrected for atmospheric effects (ionosphere, wet and dry troposphere), effects due to surface conditions (electromagnetic bias), and other contributions (ocean tides, pole tide, and inverse barometer). The value of the mean sea surface used to calculate SSA is from the mean sea surface height fields by *Rapp et al.* [1994] computed using Deos3, Seasat, and about 15 months of T/P altimeter data [*Berwin and Benada*, 2000]. For the purpose of the present study, the along-track data are first mapped on a regular $1° \times 1°$ grid using a Gaussian interpolation scheme and averaged per month afterward.

2.3. Model-Data Comparison
2.3.1. Mean and Seasonal Cycle

[13] In order to validate the FLAME model, mean sections at 35°W and at/near 23°W from SPFLAME as well as from observations [*Schott et al.*, 2003; *Brandt et al.*, 2006] are considered (Figure 1). The mean sections from the models are evaluated for transports in isopycnal layers according to the observations, but because of a too shallow $\sigma_\theta = 24.5$ kg/m^3, isopycnal in the FLAME model $\sigma_\theta = 25.4$ kg/m^3 is chosen instead as a lower boundary of the surface layer. This feature can primarily be ascribed to a too diffuse thermocline as already noted by *Schott and Böning* [1991] for the CME model. Besides, individual EUC transport estimates from observations at 35°W and at/near 23°W are calculated by taking only eastward velocities into account for both the density range $\sigma_\theta = 24.5–26.8$ kg/m^3 and the depth range 30–300 m. Mean transports are derived by averaging the individual section transports, and uncertainties are estimated from the standard deviation of EUC transports assuming independent individual realizations (Table 1). The transports

for the density range are somewhat smaller compared to the ones for the depth range; thus some eastward transport above $\sigma_\theta = 24.5$ kg/m^3 is missed by the chosen density range. In order to capture the total range of EUC transport variability from observations, the transports for the 30- to 300-m depth range are chosen here. Figure 2 presents these individual transport estimates at 35°W and at/near 23°W in comparison with the respective seasonal cycles of EUC transport from both models, calculated from the eastward zonal velocities between $±2.5°$ in latitude and within the layer 31.5–310.6 m by monthly averaging.

2.3.1.1. 35°W Section

[14] The mean 35°W zonal velocity section from 16 cruises shows the EUC centered at the equator, with its core at about 100-m depth and a maximum velocity of about 65 cm/s. The EUC transport calculated from the mean velocity section amounts to 19.9 Sv, with 5.3 Sv in the surface layer and 14.6 Sv in the thermocline layer $\sigma_\theta = 24.5–26.8$ kg/m^3. Although the mean EUC transport at 35°W from the FLAME model (19.2 Sv) is in good agreement with the value derived from observations, the transport distribution between surface and thermocline layer is different, i.e., of nearly equal magnitude. This difference is mainly due to a shallower model EUC core, located slightly south of the equator at about 70-m depth in the surface layer. In case of the SPFLAME model, the vertical extent of the EUC is, particularly toward the surface, much diminished compared to the FLAME model and the observations. But in agreement with the observations, the core of the SPFLAME EUC is found in the thermocline layer at about 100-m depth. Because of its shrunken upper part, the EUC transports here only 2.8 Sv in the surface layer and 11.1 Sv in the thermocline layer. The too deep SPFLAME EUC also results in significant differences concerning the westward surface flow. While the FLAME model and the observations show two separated bands of westward flow in the surface layer, the SPFLAME model has just a broad band of westward surface flow. Note that the EUC in both models is not clearly separated from the South Equatorial Undercurrent (SEUC) in the thermocline layer as indicated by the observations.

[15] The seasonal cycle of EUC transport at 35°W from the FLAME model is characterized by two transport maxima of about equal magnitude during March/April and September. On the other hand, the seasonal cycle of EUC transport in the SPFLAME model run shows a maximum during April and another during November. But EUC transports obtained from 15 cross-equatorial sections at 35°W are in reasonable agreement with both simulated seasonal cycles, with the largest discrepancies during June 1991 and September 1995. Because of the limited number of measurements, the EUC transport observations do not allow us to evaluate the quality of the simulated seasonal cycles of both model runs.

2.3.1.2. 23°W Section

[16] As pointed out by *Brandt et al.* [2006], the EUC loses some 6 Sv over about 1000 km of equatorial extent between 35°W and about 23°W. This reduction is well reproduced by the FLAME model, with an EUC transport of 13.7 Sv across 23°W compared to 19.2 Sv across 35°W. The differences concerning the characteristics of the mean EUC core from observations and the FLAME model, as noted above for the comparison of the mean 35°W sections, are also apparent in the central Atlantic. But the observed
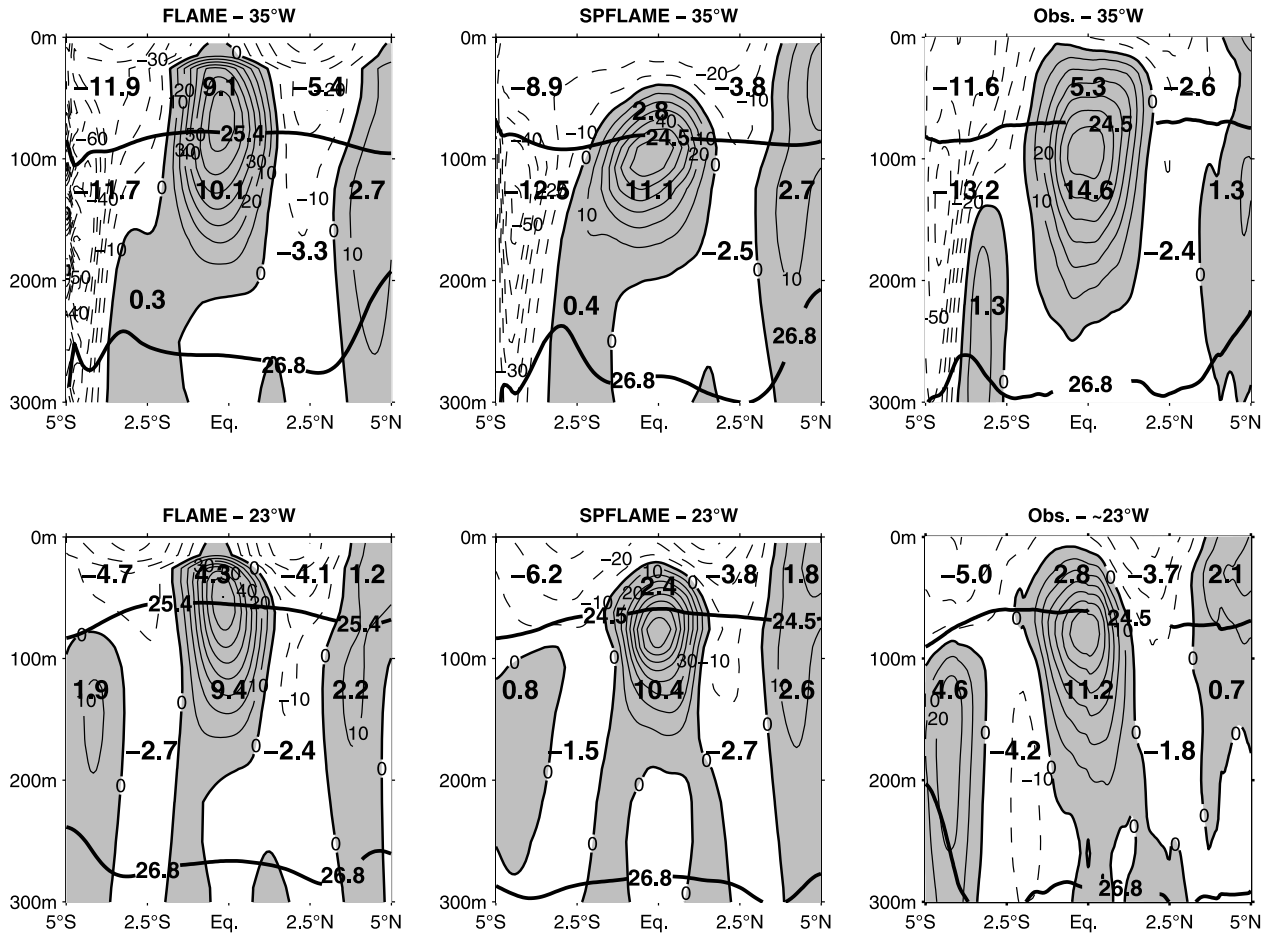
Figure 1. Upper panels: Mean zonal velocity (contour interval is 10 cm/s) at 35°W from FLAME (left), SPFLAME (middle), and from 16 ship sections [*Schott et al.*, 2003; *Brandt et al.*, 2006] (right), with layer transports (Sv= 10^6 m³/s) of different current branches overlaid on potential density (thick solid lines). Lower panels: Mean zonal velocity (contour interval is 10 cm/s) at/near 23°W from FLAME (left), SPFLAME (middle), and from 13 ship sections [*Brandt et al.*, 2006] (right), with layer transports (Sv) of different current branches overlaid on potential density (thick solid lines).

and simulated EUC transport distributions between surface and thermocline layer are in better agreement in the central equatorial Atlantic than near the western boundary. Contrary to the observations, the EUC transport in the SPFLAME model run stays fairly constant, with 12.8 Sv across 23°W compared to 13.9 Sv across 35°W. However, the shape of the SPFLAME EUC is in an overall better agreement with the observations in the central equatorial Atlantic. To the north and south of both observed and simulated EUC, two branches of the westward South Equatorial Current (SEC) are present in the surface layer, and the corresponding westward transports are of comparable magnitude. Contrary to the 35°W section, the SEUC is clearly separated from the EUC at 23°W in both simulations, and its eastward transport amounts to 1.9 and 0.8 Sv in the thermocline layer of the FLAME and SPFLAME model, respectively. In agreement with the mean sections from observations, the simulated SEUCs increase toward the east, but the model transports are significantly lower than observed.

[17] Considering the seasonal cycle of EUC transport at 23°W from the FLAME model, transport maxima during

September and April as well as minima during February and May/June are apparent. While the simulated maxima at 35°W are of nearly equal magnitude, the September maximum is significantly stronger compared to the April one at 23°W. Contrary to the 35°W section, the simulated seasonal cycles of EUC transport from FLAME and SPFLAME are in general agreement in the central equatorial Atlantic. Individual EUC transports are derived from nine cross-equatorial sections carried out between 29°W and 23°W. These snapshot transports exhibit a large range of variability that prevents from establishing a definite seasonal cycle from observations. In particular, one of the highest transport estimates is obtained at 23°W during June 2005, coincident with a minimum of the simulated seasonal cycles.

[18] The comparison between the FLAME and SPFLAME model runs reveals significant differences concerning the annual mean and seasonal cycle of the EUC at 35°W, whereas a general agreement is found at 23°W. As first pointed out by *Pacanowski and Philander* [1981], the simulation of the equatorial upper-layer currents, and particularly the EUC, depends strongly on the parameterization of the vertical

Table 1. EUC Transports [Sv = 10^6 m³/s] in the Western and Central Equatorial Atlantic From Cross-Equatorial Ship Sections, for the Density Range σ_θ = 24.5–26.8 kg/m³ and the Depth Range 30–300 m

Cruise	Transport, Sv (24.5–26.8 kg/m³)	Transport, Sv (30–300 m)
L'Atalante, 35°W (Feb. 1993)	18.50	23.67
Ron Brown, 35°W (Feb. 2002)	15.98	20.92
Meteor, 35°W (Mar. 1994)	13.43	19.38
Oceanus, 35°W (Mar. 2001)		
Edwin A. Link, 35°W (Apr. 1996)	16.63	24.55
Meteor, 35°W (Apr. 2000)	13.44	22.58
Meteor, 35°W (May 2002)	15.02	23.98
Sonne, 35°W (May 2003)	17.50	21.81
Meteor, 35°W (Jun. 1991)	24.83	36.24
Meteor, 35°W (Jun. 2006)	17.10	23.52
Thalassa, 35°W (Jul. 1999)	13.54	17.63
Meteor, 35°W (Aug. 2004)	19.24	23.76
Le Noroit, 35°W (Sep. 1995)	23.85	35.83
Meteor, 35°W (Oct. 1990)	19.51	24.77
Meteor, 35°W (Nov. 1992)	14.76	18.63
Sonne, 35°W (Dec. 2000)	12.28	14.75
Mean	17.04 (n = 15)	23.47 (n = 15)
Standard error	0.96 (n = 15)	1.51 (n = 15)
Seward Johnson, 23°W (Jan. 2000)	10.32	15.07
Seward Johnson, 25.5°W (Jan. 2000)	10.87	17.27
Seward Johnson, 28°W (Jan. 2000)		
Meteor, 23°W (Apr. 2000)	9.77	14.19
Meteor, 28°W (May 2002)	9.23	10.47
Sonne, 28.5°W (May 2003)		
Meteor, ~23°W (May 2006)		
Polarstern, 23°W (Jun. 2005)		22.48
Meteor, 23°W (Jun. 2006)	19.41	20.17
Thalassa, 23°W (Aug. 1999)	12.81	14.73
Ron Brown, 25°W (Aug. 2003)	21.51	24.50
Meteor, 28°W (Aug. 2004)	14.70	22.01
Meteor, 24°W (Oct. 2002)		
Mean	13.58 (n = 8)	17.88 (n = 9)
Standard error	1.64 (n = 8)	1.56 (n = 9)

mixing of momentum. The strong sensitivity of the simulated EUC to the vertical viscosity is here suspected to be the main reason for differences in the representation of the simulated EUC. Apart from different vertical mixing schemes, the larger discrepancies at 35°W may be attributed to the sensitivity of the recirculation patterns near the western boundary to parameterization choices of lateral mixing as stated by *Böning and Kröger* [2005]. However, analysis of the model sensitivity to different mixing parameterizations is beyond the scope of this paper.

[19] Both at 35°W and 23°W, the simulated seasonal cycles of EUC transport from the FLAME model are in general agreement with results presented in previous studies. *Philander and Pacanowski* [1986b, Figure 3] found a maximum EUC transport during July to September at 30°W and 10°W as well as secondary maxima during March/April and January/February, respectively. Likewise, *Schott and Böning* [1991, Figure 8] at 30°W and *Hazeleger et al.* [2003, Figure 2] at 35°W and 20°W yielded comparable results. The basin-wide description of the seasonal cycle of EUC transport by *Arhan et al.* [2006, Figure 6a] also revealed two maxima, one during August to November in the basin interior and the other one during January to June, most pronounced between 40°W and 35°W near the western boundary, but extending eastward to about 10°W. A recent

study by *Hüttl and Böning* [2006, Figure 6a], also based on the FLAME hierarchy of models, yielded significant differences concerning the seasonal cycle of the EUC at 35°W in the 1/12° and 1/3° model versions. While the 1/12° case reveals the double-maximum EUC cycle (see Figure 2, upper panel), the boreal winter/spring maximum is missing in the coarser resolution case, attributed to an unrealistically weak thermocline part. These findings by *Hüttl and Böning* [2006] along with our results concerning the seasonal cycle of EUC transport at 35°W point toward the uncertainties in determining a seasonal cycle of EUC transport near the western boundary from model simulations. But evidence from observations is still limited, as exemplified in case of the 35°W and near 23°W sections. *Katz et al.* [1981], using 22 sections taken between 33°W and 25°W during the Global Weather Experiment, found the highest EUC transport during early March (based on a single section) and a secondary maximum during August. From an evaluation of the eight Programme Français Océan et Climat dans l'Atlantique Equatorial/Seasonal Response of the Equatorial Atlantic (FOCAL/SEQUAL) cruises at 23°W, *Hisard and Hénin* [1987] obtained maximum EUC transports during autumn, but time series of moored current meters at 28°W, 0° by *Weisberg et al.* [1987] during 1983–1985 did not show a detectable seasonal cycle of EUC transport.

2.3.4. Surface Velocity

[20] Inspection of longitude-time diagrams of the zonal surface velocity, averaged between ±2.5° in latitude, from the FLAME model and the drifter climatology (Figure 3) yields good agreement concerning the periods of maximum westward velocities during April to July and during November to December. But besides that, there are remarkable differences regarding periods of weakest westward or even eastward velocities particularly in the region east of 5°E. The drifter climatology reveals slightly westward velocities west of about 0° during both January to March and August to October, with an eastward velocity maximum between about 0° and 5°E during the latter period. Otherwise, the model shows mainly eastward velocities during the first quarter of the year as well as to the east of about 4°W during August to October, and largest velocities (≥20 cm/s) occur between about 4°W and 5°E during February and March. But note that despite these differences, the longitudinal averaged seasonal cycle from the FLAME model fits generally in the error margins of the drifter climatology.

2.3.5. Cold Tongue

[21] In this study, the simulated near-surface temperature in 15-m depth is chosen instead of SST because of the applied Haney-type surface heat flux relaxation [*Haney*, 1971]. The modeled SST will therefore be constrained to be close to the climatological SST, and, in particular, interannual SST variability is significantly affected. However, near-surface temperature anomalies are derived here by removing the respective seasonal cycle of the 13-year model simulation at each grid point, and Figure 4 shows a time series of the near-surface temperature anomaly within the cold tongue region 20°W–5°E, 6°S–2°N in comparison with a corresponding time series of the NOAA OI SST data set. Overall, the agreement between the two time series is reasonable (r = 0.52), with largest differences occurring in the mid-1990s. The additionally marked monthly anomaly
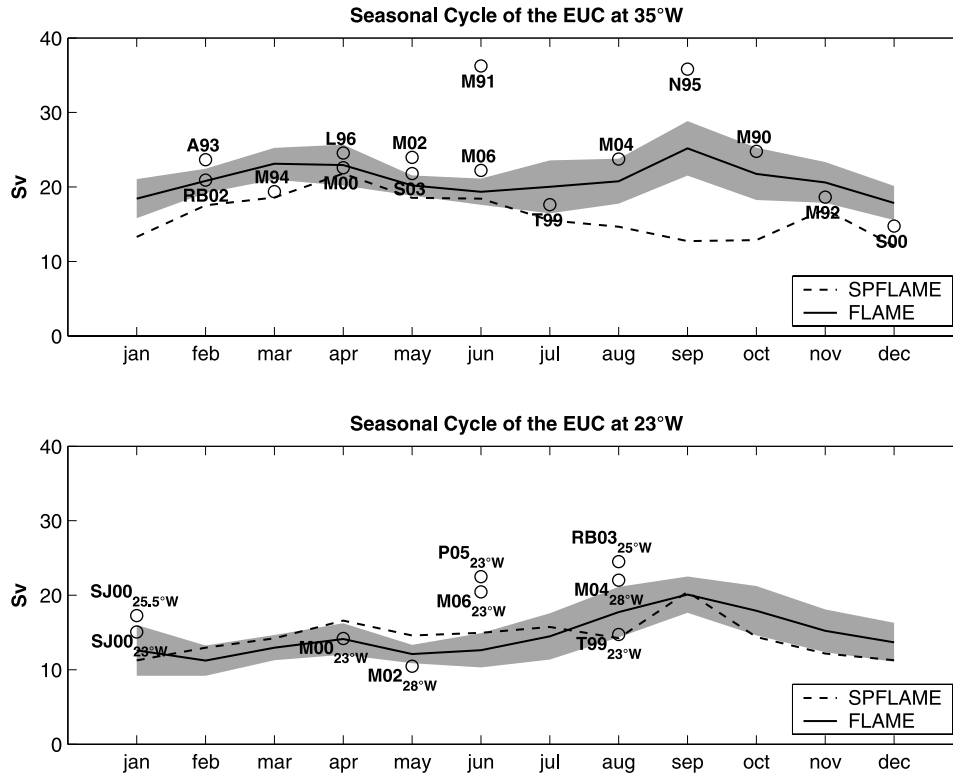
Figure 2. Upper panel: Seasonal cycle of EUC transport (Sv), calculated between ±2.5° in latitude and within the layer 31.5–310.6 m, at 35°W from FLAME (solid line) and SPFLAME (dashed line), with standard deviation for FLAME (shaded). Marked are EUC transports (Sv) from 15 cross-equatorial ship sections carried out at 35°W during 1990–2006; indicated are ship name (A = L′Atalante, RB = Ron Brown, M = Meteor, L = Edwin A. Link, S = Sonne, T = Thalassa, N = Le Noroit) and year of survey. Lower panel: Same as upper panel, but at 23°W. Marked are EUC transports (Sv) from nine cross-equatorial ship sections carried out between 29°W and 23°W during 1999–2006; indicated are ship name (SJ = Seward Johnson, M = Meteor, P = Polarstern, RB = Ron Brown, T = Thalassa), year of survey, and location.

values from the MW OI SST data set give an idea of the uncertainties inherent in the observations.

3. Mean and Seasonal Cycle

3.1. Mean Flow

[22] In order to present a view of the EUC evolution in the eastern equatorial Atlantic, Figure 5 shows the annual mean zonal velocity distributions at 10°W and 3°E from the FLAME model. In comparison to the 23°W section (Figure 1, lower left panel), the EUC has significantly weakened at 10°W. Above $\sigma_\theta = 26.8$ kg/m^3, the EUC transports only 9.2 Sv eastward, and the velocity of its core, still located slightly south of the equator at about 50-m depth, has reduced to about 65 cm/s compared with 80 cm/s at 23°W. But note that contrary to the afore-discussed 23°W section, the EUC is found here nearly completely below $\sigma_\theta = 25.4$ kg/m^3. The aforementioned two branches of the SEC are again observable in the surface layer to either side of the EUC as well as the SEUC in the thermocline layer near the southern boundary of the section. In the surface layer to the north of about 2°N, there are indications of the eastward Guinea Current. At 3°E, the overall circulation has largely weakened, and the EUC transport has reduced to 2.3 Sv, only three quarters of the transport at 10°W.

3.2. Seasonal Cycle

[23] Contrary to the afore-discussed seasonal cycles of EUC transport that are calculated for a fixed depth range, isopycnal layers are considered here for the meridional sections at 23°W, 10°W, and 3°E. Isopycnal layers are chosen because they follow the depth range of the thermocline better. The seasonal cycle of thermocline EUC transport is derived from eastward zonal velocities between ±2.5° in latitude and within the isopycnal range $\sigma_\theta = 25.4$–26.8 kg/m^3, whereas the seasonal cycle of total eastward transport is calculated between ±2.5° in latitude and above $\sigma_\theta = 26.8$ kg/m^3 (Figure 6). We differentiate here between thermocline EUC transport and total eastward transport because of the presence of eastward surface currents, particularly in the eastern equatorial Atlantic during January to March (Figure 3, upper panel).

[24] At 23°W, where a significant part of the EUC is found above $\sigma_\theta = 25.4$ kg/m^3 (Figure 1, lower left panel) and equatorial surface currents are usually westward (Figure 3, upper panel), the seasonal cycle of total eastward transport represents that of the EUC. In correspondence to Figure 2 (lower panel), the seasonal cycle of total eastward transport at 23°W is characterized by a maximum during September, a secondary maximum during April, and minima during May/June and February. The seasonal cycle of thermocline
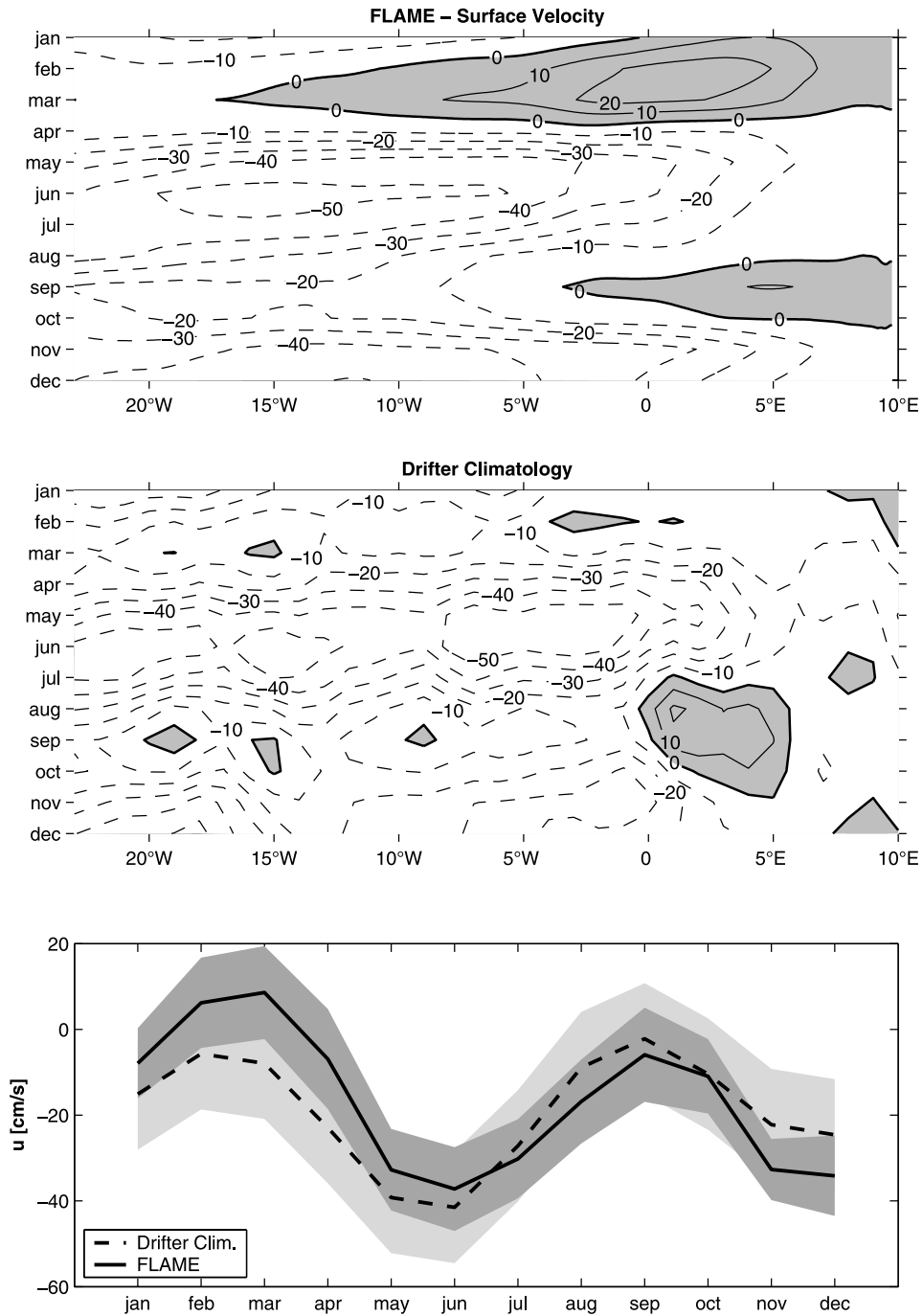
Figure 3. Longitude-time diagrams of the annual mean zonal surface velocity (contour interval is 10 cm/s), averaged between ±2.5° in latitude, from FLAME (upper panel) and the drifter climatology by *Lumpkin and Garzoli* [2005] (middle panel). Lower panel: Corresponding longitudinal averaged seasonal cycles from FLAME (solid line), with standard deviation (dark gray shaded), and the drifter climatology (dashed line), with standard error (light gray shaded).

EUC transport shows rather an annual cycle, with a maximum during August/September and a minimum during February. At 10°W, the seasonal cycles of thermocline EUC transport and total eastward transport are in close agreement except during February to April. The seasonal cycle of total eastward transport reveals maxima during September and March and minima during May and boreal winter. In

agreement with the 23°W section, the seasonal cycle of thermocline EUC transport is characterized by a maximum during September and a minimum during February/March. Overall, the seasonal cycles of both isopycnal ranges are much diminished at 3°E. But weak thermocline EUC transport maxima during February and July as well as a pronounced total eastward transport maximum during February are observable.
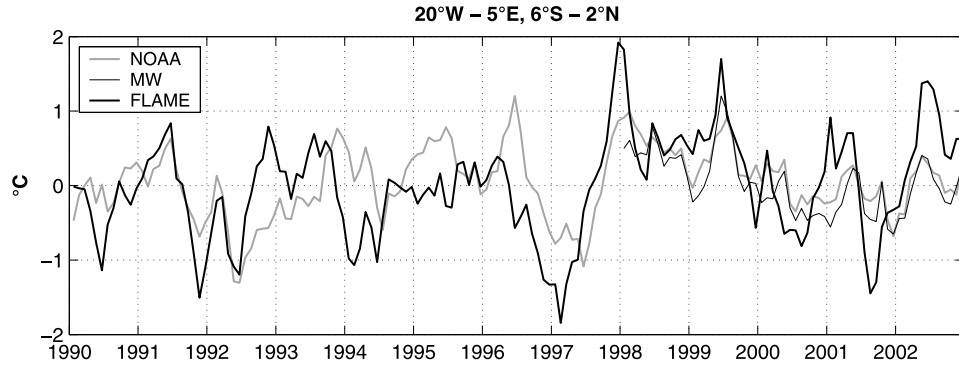
Figure 4. Time series of 15-m temperature anomalies from FLAME (thick black line), NOAA (thick gray line), and MW OI SST anomalies (thin black line; °C) within the box 20°W–5°E, 6°S–2°N.

[25] The strong thermocline EUC transport reduction compared to the total eastward transport during boreal winter/spring at all three locations suggests that the boreal winter/spring maximum is rather due to an eastward flow in the surface layer than in the thermocline layer. This feature is in agreement with recent time series from moored Acoustic Doppler Current Profilers at 23°W, 0°, revealing the EUC closer to the surface during January to May [*Provost et al.*, 2004; *Giarolla et al.*, 2005; *Brandt et al.*, 2006].

3.3. Meridional Ekman Divergence

[26] In order to study the relation between the seasonal cycle of EUC transport and wind-induced equatorial upwelling, the meridional Ekman divergence between 2.5°N and S ($T_{ek}^{2.5°N} - T_{ek}^{2.5°S}$) from the FLAME model is presented (Figure 7). The pattern can generally be described by divergences, associated with prevailing easterly winds, to the west of about 0° and convergences, due to an eastward wind stress component related to the low-pressure system on the African continent [*Du Penhoat and Treguier*, 1985], farther east. While the meridional Ekman divergence maximum during November can be found throughout the equatorial Atlantic, there are regional differences concerning another maximum during boreal spring/summer. To the east of about 15°W, this maximum shows up during April to June, whereas it appears between about 25°W and 15°W during July and farther west during August. In the central and eastern equatorial Atlantic, the meridional Ekman divergence is at minimum during August/September and February/March.

[27] However, seasonal variations of the meridional Ekman divergence are rather dominated by an annual harmonic near the western boundary, whereas a prevailing semiannual signal is apparent in the central and eastern parts of the basin (q.v. *Philander and Pacanowski* [1986a]).

[28] Obviously, the seasonal cycle of the meridional Ekman divergence is not simply related with the seasonal cycle of thermocline EUC transport, in particular, because of a remote forcing of the EUC strength. The boreal summer/autumn maximum of the EUC is regarded as a near-equilibrium response to the equatorial easterly trades in the western and central Atlantic [e.g., *Philander and Pacanowski*, 1980, 1986a], and thus a correspondence between this EUC maximum and a maximum of the meridional Ekman divergence can be expected near the western boundary during boreal summer/autumn. During February/March, the meridional Ekman divergence minimum that is present throughout the equatorial Atlantic coincides with the thermocline EUC transport minima at 23°W and 10°W as well as with the weak thermocline EUC transport maximum at 3°E. Favored by the eastward shoaling of the EUC, eastward wind stress anomalies drive directly surface and undercurrent layer in the easternmost part of the equatorial Atlantic.

3.4. Mean Box Budget

[29] For the purpose of further examining the relation between horizontal transports and upwelling, in particular, with regard to the EUC, Figure 8 (upper panel) shows an annual mean box budget of the central and eastern equato-
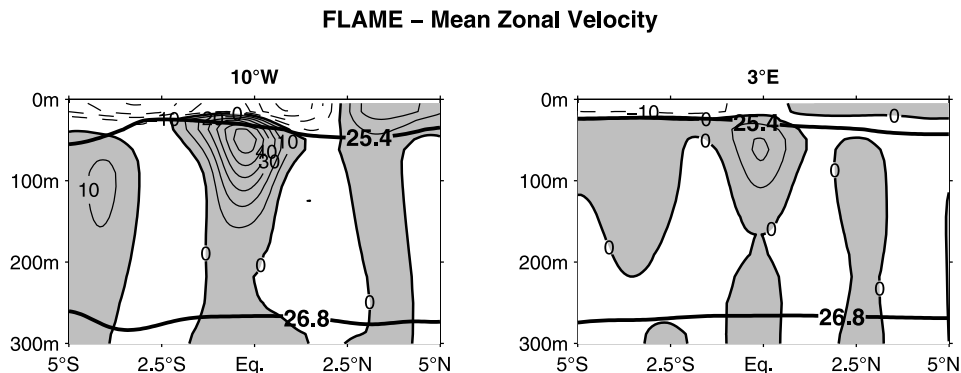
FLAME – Mean Zonal Velocity

Figure 5. Annual mean zonal velocity (contour interval is 10 cm/s) at 10°W (left panel) and 3°E (right panel) from FLAME. Marked are isopycnals $\sigma_\theta = 25.4$ and 26.8 kg/m^3 (thick solid lines).
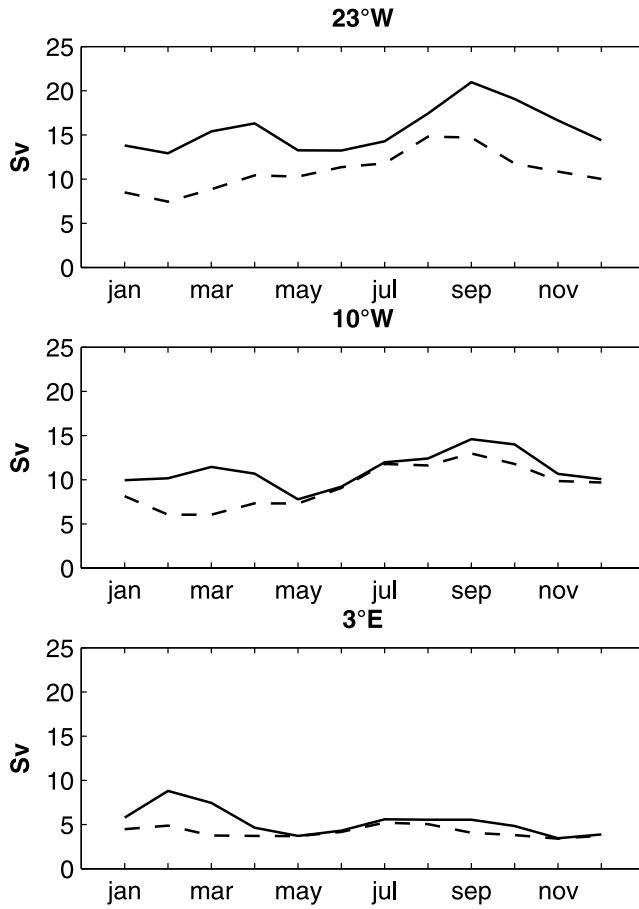
FLAME – Seasonal Cycle

Figure 6. Seasonal cycle of thermocline EUC transport (dashed lines) and total eastward transport (solid lines; Sv) at 23°W (upper panel), 10°W (middle panel), and 3°E (lower panel) from FLAME. Transports are calculated between ±2.5° in latitude and between σ_θ = 25.4–26.8 kg/m^3 in case of the thermocline EUC transport and above σ_θ = 26.8 kg/m^3 in case of the total eastward transport, respectively.

rial Atlantic calculated from the FLAME model. The boxes are defined by zonal sections at 2.5°N, 2.5°S, 7.5°S, and 15°S as well as by meridional sections at 23°W, 10°W, and 3°E, with section horizontal transports indicated for both thermocline and surface layer. These mean transports are derived by first calculating the respective transports for each time step and then averaging over the whole period. Upwelling across σ_θ = 25.4 kg/m^3, which is generally below the mixed layer, results from the continuity of the corresponding section horizontal transports of the surface layer; that is, horizontal transport divergences (convergences) lead to upwelling (downwelling).

[30] At 23°W, the thermocline layer is characterized by a strong eastward inflow in the equatorial belt (5.9 Sv) because of the EUC and a reduction of the eastward flow toward the African coast. Associated with the eastward weakening of the thermocline flow along the equator, there is significant upwelling throughout the equatorial belt. In this region, the surface layer transports are predominantly characterized by a meridional divergence west of 10°W and a zonal divergence east of 10°W. This feature is also illustrated in Figure 8 (lower panel). While the total surface layer transport divergence is mainly determined by the zonal transport divergence from the eastern boundary up to about 10°W, the meridional transport divergence contributes significantly just to the west of about 10°W. The additionally depicted annual mean meridional Ekman divergence shows weak convergences to the east of 5°W, followed by a steep increase toward the west. As discussed by *McCreary and Lu* [1994], the meridional transport in the surface layer is given by the Ekman drift and the geostrophic transport (q.v. *Schott et al.* [2004]). The geostrophic transport always counteracts the Ekman transport which is the main reason for the difference between total surface layer transport divergence and meridional Ekman divergence. However, equatorial upwelling is most intense between 10°W and 3°E (1.5 Sv), coincident with strongest thermocline EUC transport reduction (4.3 versus 1.1 Sv). Although the eastward weakening of the EUC is in part also due to a southward transport in the thermocline layer across 2.5°S, a significant part of the EUC supplies the equatorial upwelling. The adjacent southern belt reveals also eastward transports in the thermocline layer, here attributed to the SEUC, as well as westward transports above σ_θ = 25.4 kg/m^3. As aforementioned, between 10°W and
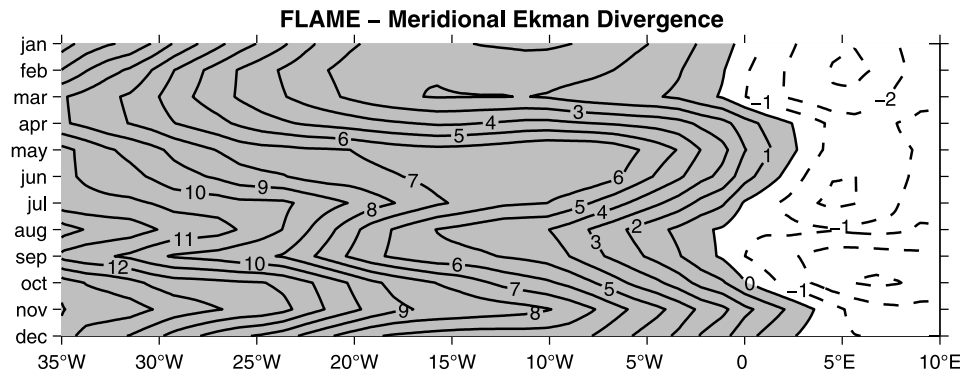

Figure 7. Longitude-time diagram of the meridional Ekman divergence between 2.5°N and S from FLAME. Contour interval is 1 m^2/s.

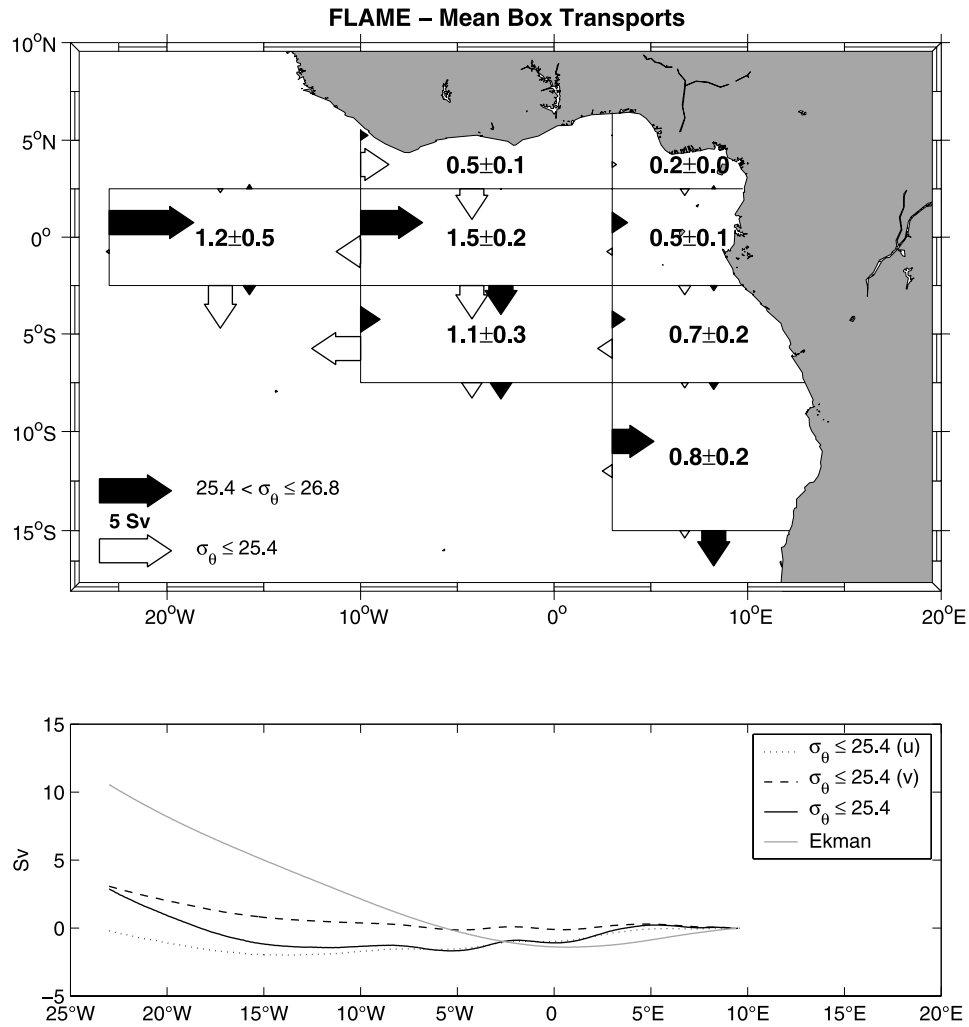**Figure 8.** Upper panel: Annual mean transports (Sv) across box boundaries from FLAME for thermocline ($\sigma_\theta = 25.4–26.8$ kg/m³; black arrows) and surface layer ($\sigma_\theta \leq 25.4$ kg/m³; white arrows), with scale indicated in the figure. Upwelling (Sv) across $\sigma_\theta = 25.4$ kg/m³, with standard deviation, is marked in box centers; positive is upward. Lower panel: Annual mean zonal (black dotted line), meridional (black dashed line), and total (black solid line) surface layer transport divergence between 2.5°N and S as well as annual mean meridional Ekman divergence between 2.5°N and S (gray solid line) from FLAME. These transport values are cumulated westward starting at the African coast.

3°E, the EUC loses some transport toward the south and thus contributes partly to the strong upwelling (1.1 Sv) between 2.5°S and 7.5°S. But besides that, the SEUC is also of importance considering the upwelling in this belt. The coastal upwelling south of 2.5°S is supplied by a weak southward flow out of the equatorial belt and eastward flow across 3°E. The southernmost box, located east of 3°E between 7.5°S and 15°S, indicates a cyclonic circulation in the thermocline layer as well as significant upwelling. These features can be associated with the Angola Dome in which center was reported at 5°E, 13°S by *Gordon and Bosley* [1991].

[31] The annual mean box budget of the central and eastern equatorial Atlantic from the FLAME model suggests a partial supply of both equatorial and coastal upwelling by the EUC. In agreement with Figure 8 (upper panel), showing that the EUC transport loss between 23°W and 10°W is mainly due to equatorial upwelling, a former study

of the tropical Atlantic's mean mass budget by *Philander and Pacanowski* [1986b] yielded that the EUC reduces its transport from 14.6 Sv across 30°W to 4.5 Sv across 10°W because of equatorial upwelling. *Philander and Pacanowski* [1986a] pointed out that the eastern equatorial Atlantic has a distinct semiannual cycle of upwelling and downwelling which is primarily associated with the divergence of the westward surface flow, not with the divergence of the meridional Ekman drift [*Philander and Pacanowski*, 1986b]. Similarly, *Verstraete* [1992] noted that neither the meridional Ekman divergence at the equator nor the coastal Ekman divergence due to alongshore winds can explain a significant part of the upwelling in the Gulf of Guinea. A concomitant analysis of thermocline water masses indicated a supply of the coastal upwelling by the EUC. *Hazeleger and de Vries* [2003] studied the fate of water masses in the Atlantic EUC using a global 1/4° ocean model and determined sites where water masses from the EUC upwell and
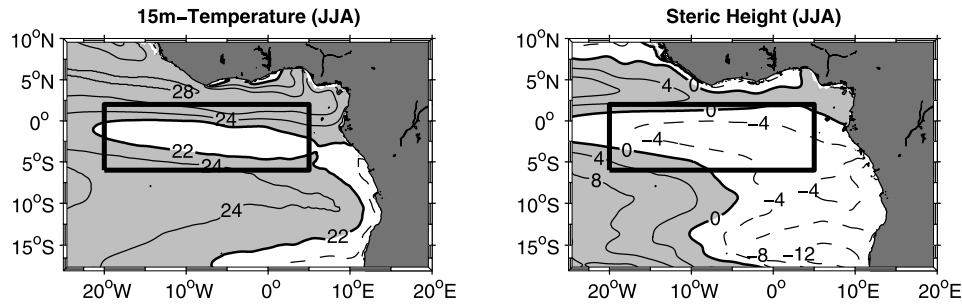
Figure 9. Mean June-July-August averages of 15-m temperature (contour interval is 2°C; left panel) and steric height (relative to about 500 m; contour interval is 4 cm; right panel) from FLAME. Marked is the box 20°W–5°E, 6°S–2°N.

later downwell by analyzing Lagrangian trajectories. In the model study by *Hazeleger and de Vries* [2003], most of the EUC water upwells in the equatorial region, although other upwelling sites are found close to the African continent.

4. Interannual Variability

4.1. Boreal Summer Cold Tongue Variability

[32] In order to further investigate the relation between zonal advection and equatorial upwelling in the Atlantic cold tongue region, we focus here on the period from June to August (JJA) when the cold tongue is most pronounced. Considering the mean June-July-August average of the near-surface temperature from the FLAME model in the central and eastern equatorial Atlantic (Figure 9, left panel), a patch of low temperatures shows up within the region 20°W–5°E, 6°S–2°N (q.v. *Xie and Carton* [2004]), and in correspondence, steric height values are also dropped in this region during boreal summer (Figure 9, right panel). For both quantities, cold tongue indices are derived by averaging the near-surface temperature and steric height anomalies of the 13-year model simulation during boreal summer over the specified region (Figures 10a and 10b). The resulting time series are highly correlated with each other ($r = 0.87$), and warm events occur generally in conjunction with positive steric height anomalies. Calculating comparable cold tongue indices from the NOAA OI SST and T/P SSA data sets (Figures 10a and 10b) confirms the close link between both time series found in the model ($r = 0.84$). Overall, there is also a reasonable agreement of the respective extrema from the model and the observations, with largest differences in the mid-1990s (see Figure 4).

[33] Figure 10c shows the June-July-August averages of the thermocline EUC transport anomalies, i.e., within the isopycnal range $\sigma_\theta = 25.4$–26.8 kg/m^3, at 35°W, 23°W, and 10°W. While the two time series at 23°W and 10°W are significantly anticorrelated with both cold tongue indices from the model, correlation coefficients, in particular, concerning the near-surface temperature-based cold tongue index, are lower regarding the thermocline EUC transport anomalies at 35°W (Table 2). Both simulated cold tongue indices are significantly correlated with the time series of the June-July-August average of equatorial zonal wind stress anomalies in the western and central Atlantic (Figure 10d). This wind time series is in turn anticorrelated with the time series of the thermocline EUC transport anomalies, i.e., stronger EUC under enhanced easterlies.

[34] In order to further illustrate the relation between extreme events and thermocline EUC transport anomalies during boreal summer, Figure 11 presents the mean June-July-August equatorial zonal velocities, zonal velocity anomalies, and potential temperature anomalies at 23°W and 10°W for three warm (1991, 1999, 2002) [cold (1990, 1992, 2001)] years occurring in conjunction with significantly reduced (enhanced) thermocline EUC transports. The warm and cold events are clearly captured by the temperature distributions, with anomalies generally more pronounced near the surface at 10°W. It is also apparent that the eastward EUC and the westward SEC north and south of the equator are weaker (stronger) during warm (cold) events. Largest anomalies are found above the EUC core, i.e., mainly above $\sigma_\theta = 25.4$ kg/m^3, at 23°W extending up to the surface. Thus westward surface velocities directly above the EUC core are enhanced (reduced) during warm (cold) events.

[35] We have shown that during boreal summer, positive (negative) near-surface temperature and steric height anomalies in the equatorial cold tongue region are linked with reduced (enhanced) thermocline EUC transports in the central and eastern Atlantic as well as weakened (increased) easterlies in the western and central part of the basin. Several studies [e.g., *Merle*, 1980; *Servain et al.*, 1982; *Zebiak*, 1993; *Ruiz-Barradas et al.*, 2000] already indicated that there is a link between SSTs in the east and surface winds in the west, and *Góes and Wainer* [2003] showed that the upper-ocean circulation decreases (intensifies) during extreme warm (cold) years, with warm events usually occurring during July.

4.2. Role of Equatorial Waves

[36] Inspection of the zonal velocity and temperature anomalies during warm and cold events showed generally largest anomalies within the surface layer (see Figure 11). Figure 12 (left panels) depicts transport anomalies of the 13-year model simulation after subtracting the mean seasonal cycle, calculated between ±2.5° in latitude and above $\sigma_\theta = 25.4$ kg/m^3 at 23°W and 10°W. The corresponding variance-conserving power spectra (Figure 12, right panels) reveal in both cases a spectral peak at a period of about 5 months, i.e., on intraseasonal timescales. Cross-correlation analyses are now carried out between these two transport time series and both near-surface temperature and steric height anomalies (Figures 13 and 14). Note that transports within the surface layer are enhanced (reduced) during warm (cold) events. The surface layer transports in the equatorial belt are
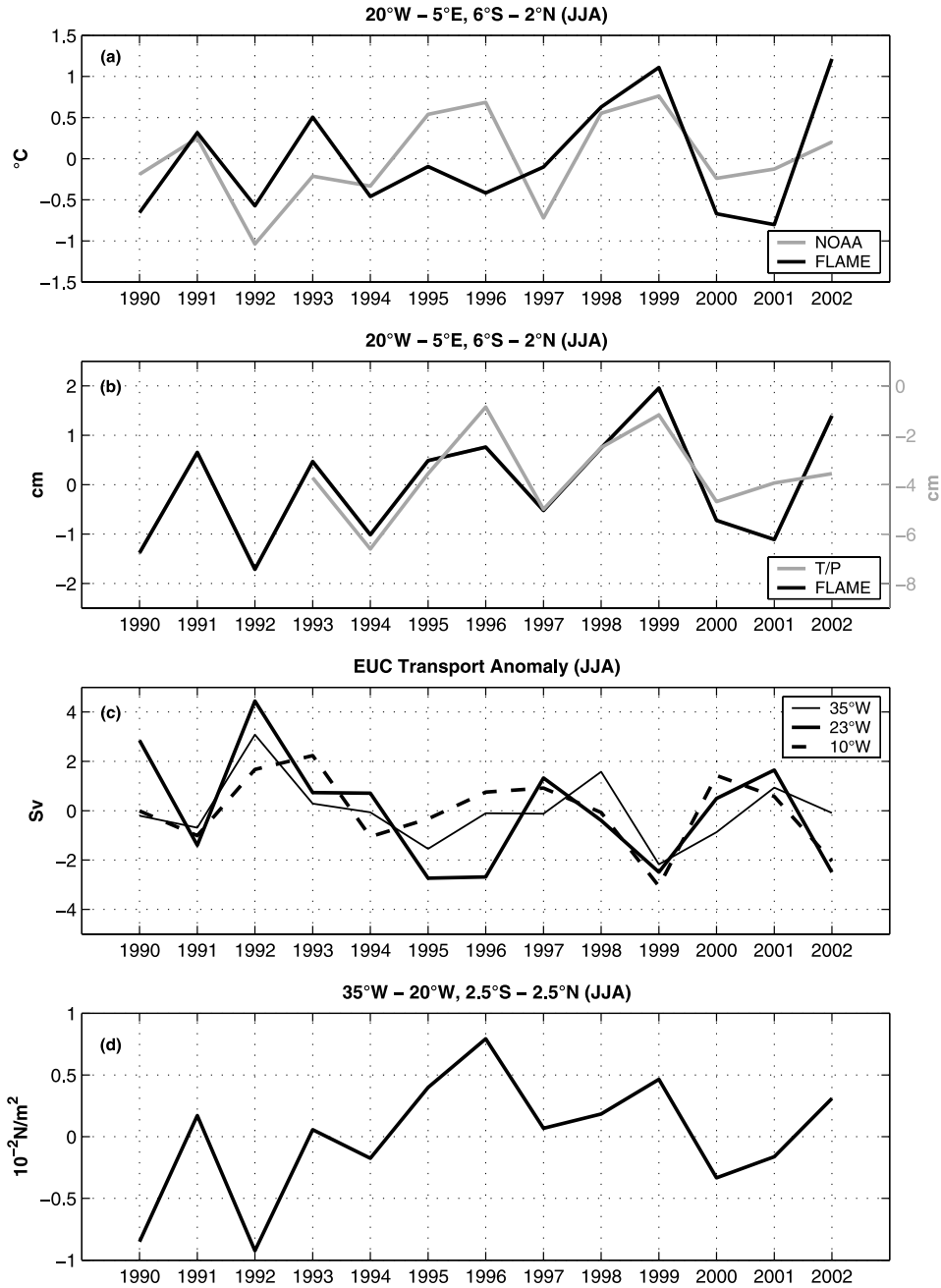
Figure 10. (a) June-July-August averages of 15-m temperature anomalies from FLAME (black line) and Reynolds' SST anomalies (gray line; °C) within the box 20°W–5°E, 6°S–2°N. (b) Same as Figure 10a, but for steric height anomalies (relative to about 500 m) from FLAME (black line) and T/P SSA (gray line; cm). (c) June-July-August averages of thermocline EUC transport anomalies from FLAME (Sv) at 35°W (thin solid line), 23°W (thick solid line), and 10°W (thick dashed line). (d) June-July-August average of zonal wind stress anomalies from FLAME (10^{-2} N/m^2) within the box 35°W–20°W, 2.5°S–2.5°N.

generally dominated by the westward SEC that weakens (strengthens) during warm (cold) events, although westward surface velocities directly above the EUC core are enhanced (reduced) during warm (cold) events (Figure 11).

[37] The cross correlation of the transport anomalies at 23°W and 10°W with near-surface temperature anomalies in the central and eastern equatorial Atlantic (Figure 13, left panels) reveals high correlations (up to 0.7) in the near-

Table 2. Correlation Coefficients Between Cold Tongue Indices (CTI) and Thermocline EUC Transport Anomalies (JJA) From FLAME at 35°W, 23°W, and 10°W[a]

	CTI$_{\theta_{15m}}$	CTI$_{SH_{500m}}$
EUC, 35°W	−0.29	−0.53
EUC, 23°W	−0.59	−0.88
EUC, 10°W	−0.59	−0.58

[a]95% and 99% significance levels are 0.51 and 0.64, respectively.
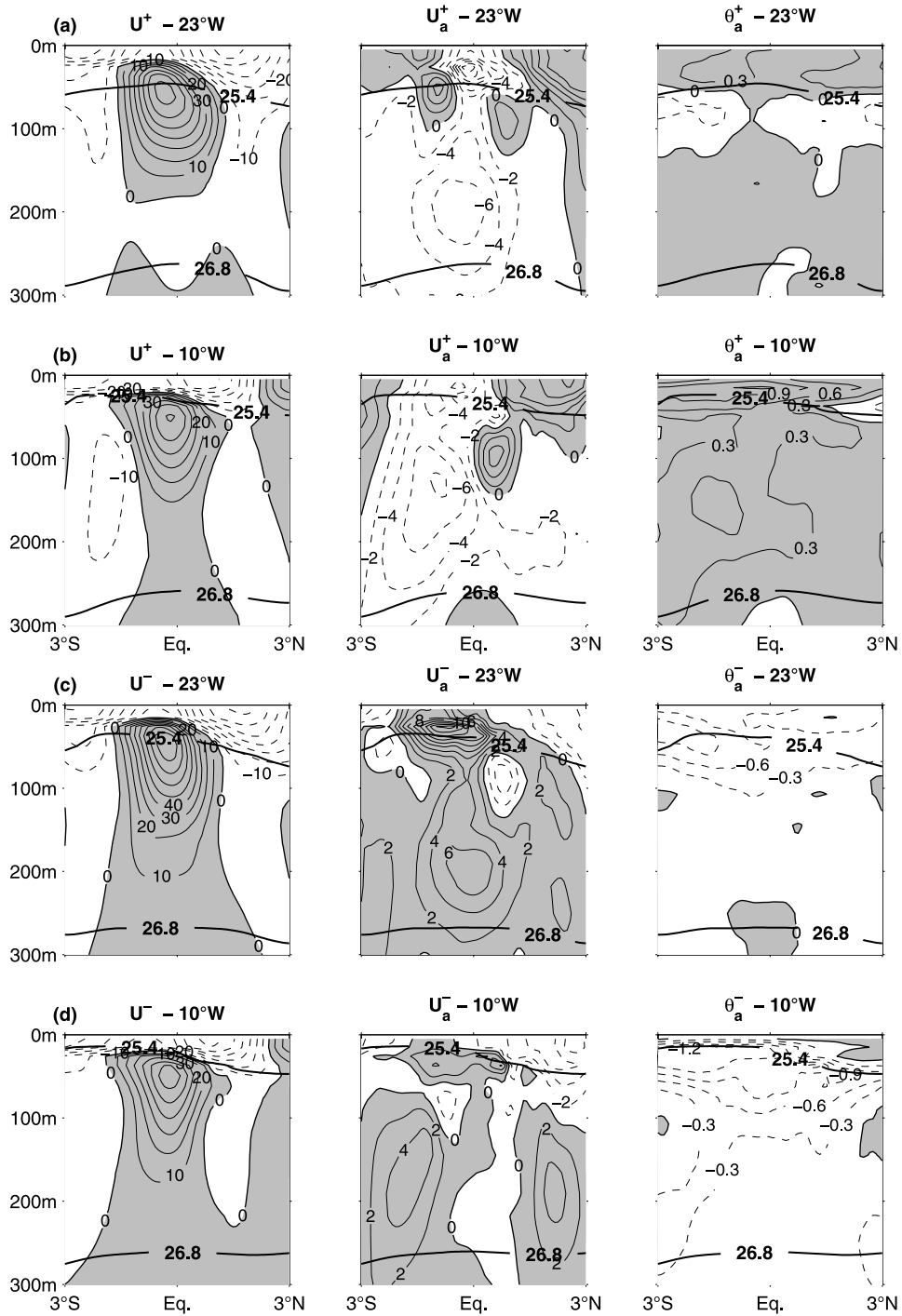
Figure 11. (a) Mean June-July-August zonal velocity (contour interval is 10 cm/s; left panel), zonal velocity anomaly (contour interval is 2 cm/s; middle panel), and potential temperature anomaly (contour interval is 0.3°C; right panel) during three warm years (1991, 1999, 2002) at 23°W from FLAME. (b) Same as Figure 11a, but for 10°W. (c) Same as Figure 11a, but for three cold years (1990, 1992, 2001). (d) Same as Figure 11c, but for 10°W.

equatorial region to the west of 10°W in the cases of both sections. Focusing on the 10°W section, somewhat weaker correlations are also found in the near-equatorial region to the east of 10°W as well as in coastal regions south of the equator. The examination of the corresponding cross correlations between the transport anomalies and steric height anomalies (Figure 13, right panels) shows significant correlations along the equator up to the African coast. Along the coast, the signal can be traced up to 10°N and 18°S, respectively. This pattern is more pronounced regarding the 10°W section, particularly in the easternmost part of the basin.
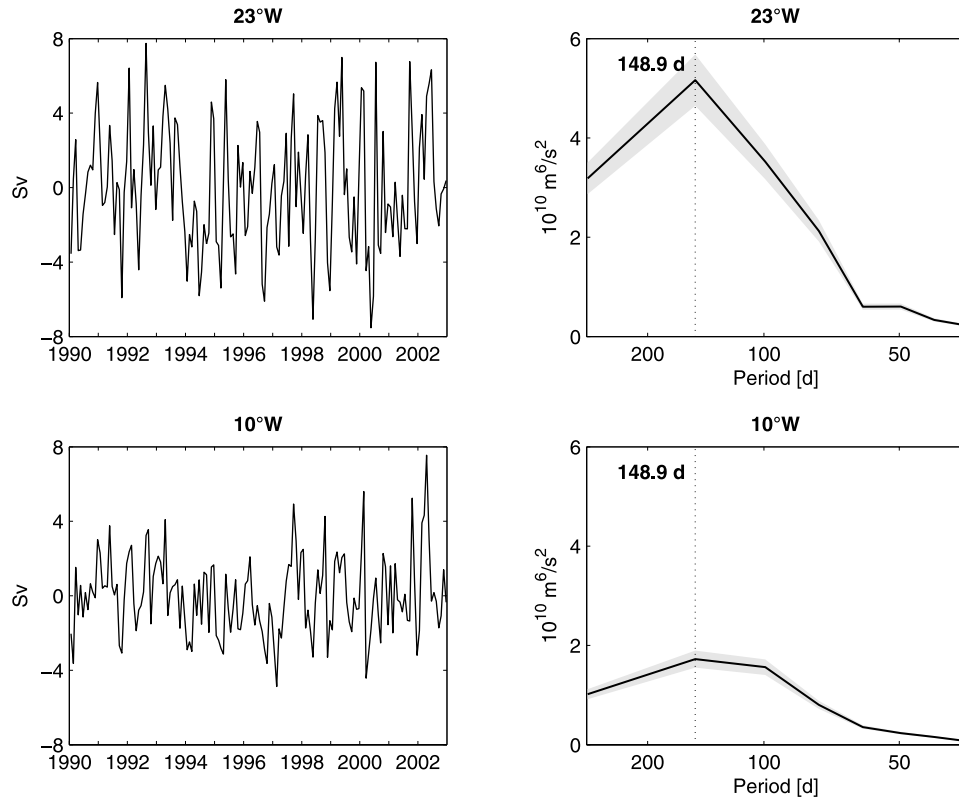
Figure 12. Left panels: Transport anomalies between ±2.5° in latitude and above $\sigma_\theta = 25.4$ kg/m^3 at 23°W (upper panel) and 10°W (lower panel) from FLAME. Right panels: Corresponding variance conserving power spectra, with 95% confidence interval (shaded).

[38] Considering the corresponding cross-correlation timescales (Figure 14), an eastward phase propagation along the equator, indicative of the presence of equatorial Kelvin waves, can be found. Note that the timescales are somewhat different: Near-surface temperature anomalies react slower to surface layer transport anomalies than steric height anomalies. This can be explained by considering the propagation of downwelling/upwelling equatorial Kelvin waves. The deepening and shallowing of the isopycnals associated with these waves act in different ways: While the steric height relative to a fixed depth (here about 500 m) is increased (reduced) in case of deeper (shallower) isopycnals, the near-surface temperature is more indirectly affected by vertical mixing leading to a reduced (increased) downward heat flux at the base of the mixed layer in case of deeper (shallower) isopycnals.

[39] At the African coast, there are differences between the two quantities as well. In the case of the steric height anomalies, the signal bifurcates into two poleward branches along the coast, and a separation from the coast as well as an associated westward phase propagation can be found between about 2–5°N and S. The correlation between the 10°W surface layer transport anomalies and the near-surface temperature anomalies shows only a westward phase propagation south of the equator, whereas the northern counterpart is missing.

[40] These cross-correlation analyses suggest a significant relation between equatorial transport anomalies within the surface layer in the central and eastern Atlantic and both near-surface temperature and steric height anomalies in the cold tongue and coastal upwelling regions. Our findings are also confirmed by a corresponding coherence analysis at a period of about 5 months (not shown) where both transport time series show their energy maxima (see Figure 12, right panels).

5. Summary and Discussion

[41] The 1/12° FLAME model of the Atlantic ocean was used here to study the EUC and associated cold tongue variability. It was shown that the FLAME model is generally in line with mean zonal velocity sections derived from ship observations at 35°W and near 23°W, with mean EUC transports of 19.2 and 13.7 Sv compared to 19.9 and 14.0 Sv from the observations. Considering the aspect of different vertical mixing parameterizations, FLAME was also compared to the SPFLAME run. While significant differences emerged at 35°W concerning the mean zonal velocity distribution and seasonal cycle of EUC transport, a general agreement was found at 23°W. Large discrepancies concerning the seasonal cycle of EUC transport at 35°W were also obtained by *Hüttl and Böning* [2006] using model simulations with different horizontal resolutions. Studying the seasonal variability of deep currents in the equatorial Atlantic, *Böning and Kröger* [2005] stated that in contrast to the zonal flow patterns in the interior, the recirculation patterns near the western boundary appear sensitive to model resolution and parameterization choices. However, because of the limited number of observations, a clear
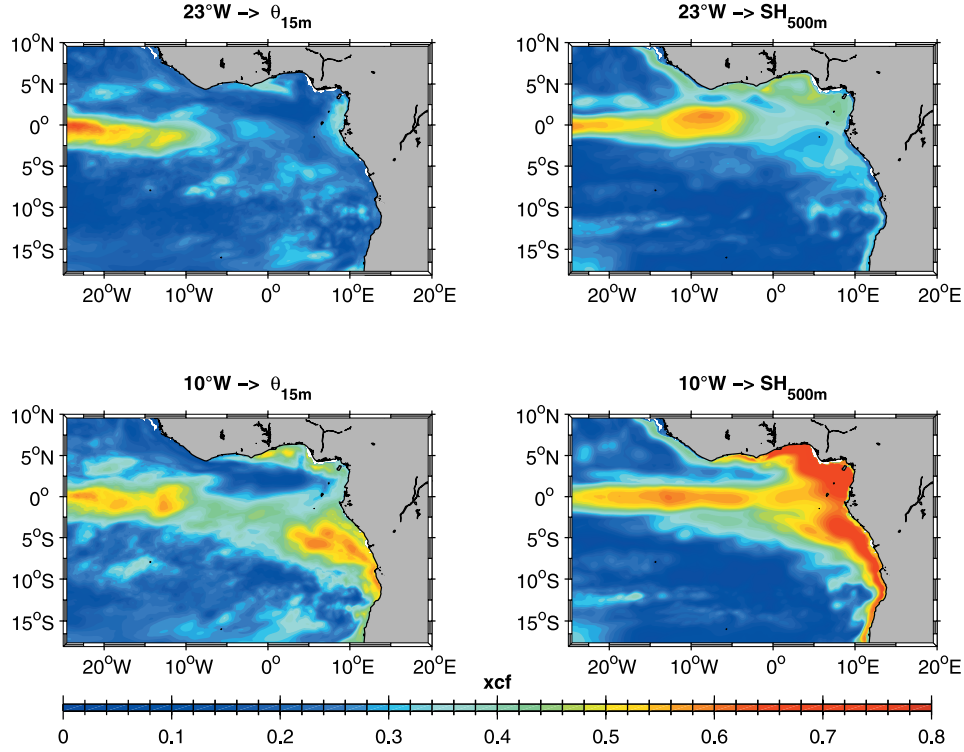
FLAME – Cross Correlation

Figure 13. Cross correlation of transport anomalies, calculated between ±2.5° in latitude and above $\sigma_\theta = 25.4$ kg/m^3, at 23°W (upper panels), and 10°W (lower panels) with 15-m temperature (left panels) and steric height anomalies (relative to about 500 m; right panels) in the central and eastern equatorial Atlantic from FLAME (95% confidence interval is 0.16).
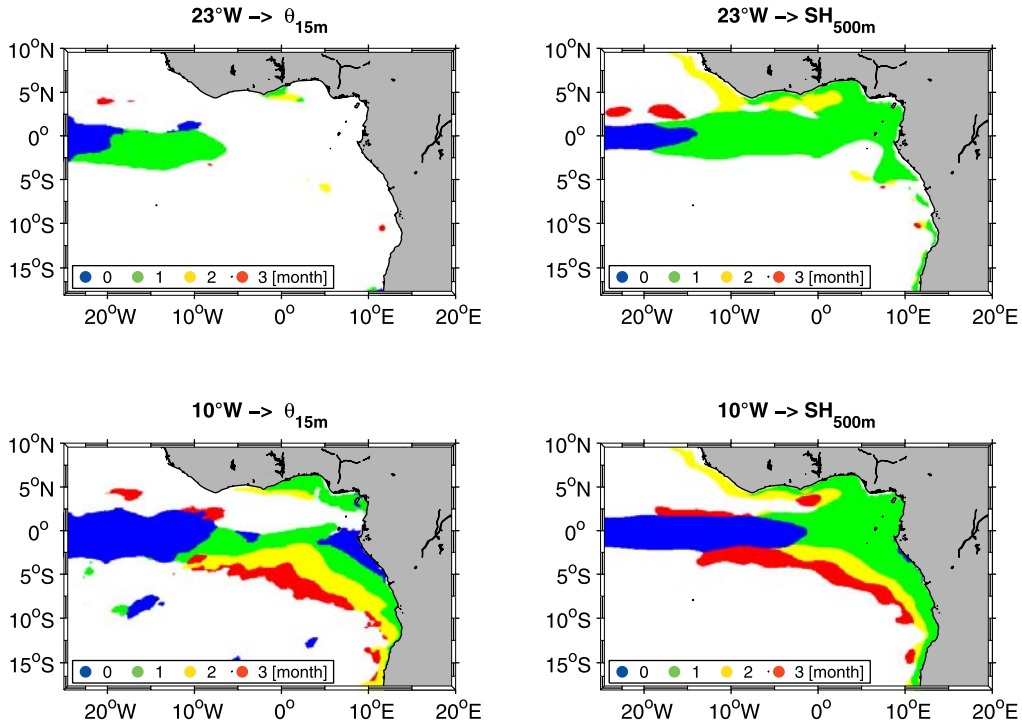
FLAME – Cross Correlation Lags

Figure 14. Cross-correlation lags (month) corresponding to Figure 13, shown only for cross correlations ≥2 × 95% upper confidence bound and lags ≥ 0.

seasonal cycle of EUC transport based on cross-equatorial ship sections is still not derivable.

[42] A clear eastward weakening of the simulated FLAME EUC is apparent throughout the equatorial Atlantic. The seasonal cycle of total eastward transport is generally characterized by two distinct maxima, one during boreal summer/autumn and another during boreal winter/spring, but only the boreal summer/autumn maximum is found concerning the thermocline EUC transport. In the easternmost part of the equatorial Atlantic, there is additionally a weak boreal winter/spring maximum in the thermocline layer that corresponds to an Ekman divergence minimum, and a forcing by local eastward wind stress anomalies is suggested.

[43] The simulation of the equatorial upper-layer currents, particularly the EUC, depends strongly on the parameterization of the vertical mixing of momentum [*Pacanowski and Philander*, 1981; *Wacongne*, 1989; *Blanke and Delecluse*, 1993]. Differences in the representation of the surface mixed layer were suspected to be a main reason for variations in the strength and eastward penetration of the EUC in the DYNAMO models [*Dynamo Group*, 1997]. The strong sensitivity of the simulated EUC to the vertical viscosity was confirmed by *Böning and Kröger* [2005, Figure 2] considering several test runs with different parameterizations of the near-surface vertical mixing. Nevertheless, the simulated eastward weakening of the EUC, in particular, in the eastern equatorial Atlantic, is consistent with several observations in this region [e.g., *Henin et al.*, 1986; *Hisard and Hénin*, 1987; *Gouriou and Reverdin*, 1992; *Bourlès et al.*, 2002; *Mercier et al.*, 2003]. This weakening of the EUC was explained as closely related to thermocline shoaling, equatorial upwelling, and enhanced vertical mixing [*Wacongne*, 1989; *Peterson and Stramma*, 1991; *Gouriou and Reverdin*, 1992].

[44] While the boreal summer/autumn maximum is a common and well-understood feature of the Atlantic EUC, regarded as a near-equilibrium response to the equatorial easterly trades in the western and central part of the basin [e.g., *Philander and Pacanowski*, 1980, 1986a], the causes of the boreal winter/spring maximum are less evident. In particular, different mechanisms seem to be at play in the easternmost part of the equatorial Atlantic and the regions to the west. The study by *Arhan et al.* [2006], showing the secondary EUC transport maximum most pronounced near the western boundary, suggested remote forcing by the low-latitude rotational wind component as well as supply from the western boundary currents. *Hisard and Hénin* [1987] observed a much more rapid eastward weakening of the EUC around 4°W during summer and autumn than during winter and spring, and a survey of the subsurface salinity maximum associated with the EUC core suggested also a deeper penetration of the EUC in the Gulf of Guinea during the latter two seasons. In this context, the seasonal migration of the zonal wind reversal in the Gulf of Guinea is believed to be of importance. The zonal winds in the Gulf of Guinea change from easterly to westerly near 4°W in the annual mean, but this reversal migrates westward with the northward movement of the intertropical convergence zone. It is expected that the associated reversal of the zonal pressure gradient migrates with the wind reversal, leading to an earlier termination of the EUC during boreal summer and autumn [*Philander and Pacanowski*, 1986a; *Hisard and Hénin*, 1987].

[45] The annual mean upwelling in the central and eastern equatorial Atlantic is found to be supplied by the EUC, but the SEUC contributes as well. In the equatorial belt, the surface layer transports are predominantly characterized by a meridional divergence west of 10°W and a zonal divergence east of 10°W.

[46] As a major contribution of the present study, a significant anticorrelation between EUC transport anomalies in the central and eastern equatorial Atlantic and both near-surface temperature and steric height anomalies in the cold tongue region is found during boreal summer. The derived cold tongue indices are also linked with equatorial zonal wind stress anomalies in the western and central part of the Atlantic basin, i.e., positive (negative) near-surface temperature and steric height anomalies in the equatorial cold tongue region occur in conjunction with weakened (enhanced) easterlies to the west. Consequently and in agreement with the dynamics of the EUC, the EUC is reduced (enhanced) while the winds relax (intensify).

[47] In order to investigate the existence and seasonality of a coupled variability similar to ENSO in the equatorial Atlantic, a recent study by *Keenlyside and Latif* [2007] discussed the individual components of the Bjerknes feedback in the Atlantic. They concluded that a weak Bjerknes feedback exists in the Atlantic, only active during boreal spring and summer. The Bjerknes feedback which may be established on a timescale of 1 to 2 months can amplify SST anomalies in the cold tongue region. Our analysis of the cold tongue season confirms these findings. Warm events are generally found to occur in conjunction with relaxed easterlies to the west of the equatorial cold tongue which in turn are linked with reduced EUC transports. Thus the supply of cold thermocline waters to the equatorial upwelling regions weakens leading to a further warming of the cold tongue. In the Pacific, a pronounced variability of the EUC is known to occur in association with El Niño, including a complete shutoff of the EUC during the largest events [*Johnson et al.*, 2002; *Izumo*, 2005].

[48] Another main point here are the results of the cross-correlation analyses between equatorial transport anomalies above $\sigma_\theta = 25.4$ kg/m^3 at 23°W and 10°W, with a spectral peak at a period of about 5 months, and both near-surface temperature and steric height anomalies in the central and eastern Atlantic. Significant correlations are found in the equatorial and coastal upwelling regions, and the corresponding cross-correlation timescales point at an eastward phase propagation along the equator toward the African coast where the signal bifurcates into two poleward branches along the coast. A separation from the coast and an associated westward phase propagation are found between 2–5°N and S. This propagation pattern suggests the presence of equatorial waves. The linear equatorial wave reflection theory indicates that an eastward propagating equatorial Kelvin wave impinging on a meridional east coast would be reflected into symmetrical westward propagating Rossby waves and coastal Kelvin waves [*Moore and Philander*, 1976]. In consistency with these theoretical considerations, *França et al.* [2003] yielded a significant lag correlation between Kelvin and first meridional mode Rossby waves near the African coast from altimetry.

[49] Model studies suggest different mechanisms creating SST anomalies in the cold tongue region, among them are air-

sea fluxes and subsurface processes as well as horizontal temperature advection [*Peter et al.*, 2006]. Of particular importance for the mixed layer heat budget seems to be the dynamics associated with tropical instability waves (TIWs) as shown by *Jochum and Murtugudde* [2006]. However, observational data are up to now not sufficient enough to close the mixed layer heat budget in the cold tongue region especially on interannual timescales. In the present study, we have analyzed the Atlantic EUC and associated cold tongue variability using the high-resolution FLAME model. While the available cross-equatorial ship sections are very useful for determining the mean flow and possibly also the seasonal cycle of EUC transport, simulated interannual EUC transport variability can only be verified by moored observations mainly because of the large intraseasonal variability that is typically not captured by shipboard measurements.

References

Arhan, M., A. M. Treguier, B. Bourlès, and S. Michel (2006), Diagnosing the annual cycle of the Equatorial Undercurrent in the Atlantic Ocean from a general circulation model, *J. Phys. Oceanogr.*, 36, 1502–1522.

Barnier, B., L. Siefridt, and P. Marchesiello (1995), Thermal forcing for a global ocean circulation model using a three-year climatology of ECMWF analysis, *J. Mar. Syst.*, 6, 363–380.

Berwin, R. W., and J. R. Benada (2000), *TOPEX/POSEIDON Sea Surface Anomaly Product*, User's Reference Manual, Version 1.0, Physical Oceanography Distributed Active Archive Center.

Bjerknes, J. (1969), Atmospheric teleconnections from the equatorial Pacific, *Mon. Weather Rev.*, 97, 163–172.

Blanke, B., and P. Delecluse (1993), Variability of the tropical Atlantic Ocean simulated by a general circulation model with two different mixed-layer physics, *J. Phys. Oceanogr.*, 23, 1363–1388.

Böning, C. W., and F. O. Bryan (1996), Large-scale transport processes in high-resolution circulation models, in *The Warmwatersphere of the North Atlantic Ocean*, edited by W. Krauss, pp. 91–128, Gebr. Borntraeger, Berlin, Stuttgart.

Böning, C. W., and J. Kröger (2005), Seasonal variability of deep currents in the equatorial Atlantic: A model study, *Deep Sea Res., Part I*, 52, 99–121.

Bourlès, B., M. D'Orgeville, G. Eldin, Y. Gouriou, R. Chuchla, Y. du Penhoat, and S. Arnault (2002), On the evolution of the thermocline and subthermocline eastward currents in the Equatorial Atlantic, *Geophys. Res. Lett.*, 29(16), 1785, doi:10.1029/2002GL015098.

Boyer, T. P., and S. Levitus (1997), *Objective analyses of temperature and salinity for the world ocean on a 1/4 degree grid*, NOAA Atlas NESDIS 11, U.S. Govt. Print. Off., Washington, D. C.

Brandt, P., F. A. Schott, C. Provost, A. Kartavtseff, V. Hormann, B. Bourlès, and J. Fischer (2006), Circulation in the central equatorial Atlantic-mean and intraseasonal to seasonal variability, *Geophys. Res. Lett.*, 33, L07609, doi:10.1029/2005GL025498.

Bryan, F. O., and W. R. Holland (1989), A high resolution simulation of the wind-and thermohaline-driven circulation in the North Atlantic Ocean. Parameterization of small-scale processes, in *'Aha Huliko'a, Hawaiian Winter Workshop*, edited by P. Müller and D. Henderson, pp. 99–115, Hawaii Institute Geophysics Spec. Publ.

Chang, P., et al. (2006), Climate fluctuations of tropical coupled systems—The role of ocean dynamics, *J. Clim.*, 19, 5122–5174.

Dengg, J., C. Böning, U. Ernst, R. Redler, and A. Beckmann (1999), Effects of an improved model representation of overflow water on the subpolar North Atlantic, *Int. WOCE Newsl.*, 37, 10–15.

du Penhoat, Y., and A. M. Treguier (1985), The seasonal linear response of the tropical Atlantic Ocean, *J. Phys. Oceanogr.*, 15, 316–329.

Dynamo Group (1997), *DYNAMO Dynamics of North Atlantic models: simulation and assimilation with high resolution models*, Berichte aus dem Institut für Meereskunde 294, IfM Kiel.

Eden, C. (2006), Mid-depth equatorial tracer tongues in a model of the Atlantic Ocean, *J. Geophys. Res.*, 111, C12025, doi:10.1029/2006JC003565.

Eden, C., and C. W. Böning (2002), Sources of eddy kinetic energy in the Labrador Sea, *J. Phys. Oceanogr.*, 32(12), 3346–3363.

Foltz, G. R., S. A. Grodsky, J. A. Carton, and M. J. McPhaden (2003), Seasonal mixed layer heat budget of the tropical Atlantic Ocean, *J. Geophys. Res.*, 108(C5), 3146, doi:10.1029/2002JC001584.

França, C., I. Wainer, A. Mesquita, and G. Goni (2003), Planetary equatorial trapped waves in the Atlantic Ocean from TOPEX/POSEIDON altimetry, in *Interhemispheric Water Exchange in the Atlantic Ocean*, edited by G. J. Goni and P. Malanotte-Rizzoli, pp. 213–232, Elsevier Oceanographic Series.

Fratantoni, D. M., W. E. Johns, T. L. Townsend, and H. E. Hurlburt (2000), Low-latitude circulation and mass transport pathways in a model of the tropical Atlantic Ocean, *J. Phys. Oceanogr.*, 30, 1944–1966.

Ganachaud, A., and C. Wunsch (2001), Improved estimates of global ocean circulation, heat transport and mixing from hydrographic data, *Nature*, 408, 453–457.

Gaspar, P., Y. Gregoris, and J.-M. Lefevre (1990), A simple eddy kinetic energy model for simulations of the oceanic vertical mixing: Tests at station Papa and Long-Term Upper Ocean Study site, *J. Geophys. Res.*, 95, 16,179–16,193.

Giannini, A., R. Saravanan, and P. Chang (2003), Oceanic forcing of Sahel Rainfall on interannual to interdecadal time scales, *Science*, 302, 1027–1030.

Giarolla, E., P. Nobre, M. Malagutti, and P. Pezzi (2005), The Atlantic Equatorial Undercurrent: PIRATA observations and simulations with GFDL Modular Ocean model at CPTEC, *Geophys. Res. Lett.*, 32, L10617, doi:10.1029/2004GL022206.

Góes, M., and I. Wainer (2003), Equatorial currents transport changes for extreme warm and cold events in the Atlantic Ocean, *Geophys. Res. Lett.*, 30(5), 8006, doi:10.1029/2002GL015707.

Gordon, A. L., and K. T. Bosley (1991), Cyclonic gyre in the tropical South Atlantic, *Deep Sea Res.*, 38(Suppl. 1), 323–343.

Gouriou, Y., and G. Reverdin (1992), Isopycnal and diapycnal circulation of the upper equatorial Atlantic Ocean in 1983–1984, *J. Geophys. Res.*, 22, 25,165–25,179.

Gu, D., and S. G. H. Philander (1997), Interdecadal climate fluctuations that depend on exchanges between the tropics and extratropics, *Science*, 272, 805–808.

Haney, L. (1971), Surface thermal boundary conditions for ocean circulation models, *J. Phys. Oceanogr.*, 1, 241–248.

Hazeleger, W., and P. de Vries (2003), Fate of the Equatorial Undercurrent in the Atlantic, in *Interhemispheric Water Exchange in the Atlantic Ocean*, edited by G. J. Goni and P. Malanotte-Rizzoli, pp. 175–191, Elsevier Oceanographic Series.

Hazeleger, W., P. de Vries, and Y. Friocourt (2003), Sources of the Equatorial Undercurrent in the Atlantic in a high-resolution ocean model, *J. Phys. Oceanogr.*, 33, 677–693.

Henin, C., P. Hisard, and B. Piton (1986), *Observations hydrologiques dans l'océan Atlantique équatorial (juillet 1982-août 1984)*, FOCAL Vol. 1, Editions de l'O.R.S.T.O.M., Collection Travaux et Documents No. 196, Paris.

Hisard, P., and C. Hénin (1987), Response of the equatorial Atlantic Ocean to the 1983–1984 wind from the Programme Français Océan et Climat Dans l'Atlantique Equatorial cruise data set, *J. Geophys. Res.*, 92(C4), 3759–3768.

Hüttl, S., and C. W. Böning (2006), Mechanisms of decadal variability in the shallow subtropical-tropical circulation of the Atlantic Ocean: A model study, *J. Geophys. Res.*, 111, C07011, doi:10.1029/2005JC003414.

Inui, T., A. Lazar, P. Malanotte-Rizzoli, and A. Busalacchi (2002), Wind stress effects on subsurface pathways from the subtropical to tropical Atlantic, *J. Phys. Oceanogr.*, 32, 2257–2276.

Izumo, T. (2005), The equatorial undercurrent, meridional overturning circulation, and their roles in mass and heat exchanges during El Niño events in the tropical Pacific Ocean, *Ocean Dyn.*, 55(2), 110–123.

Jochum, M., and R. Murtugudde (2006), Temperature advection by tropical instability waves, *J. Phys. Oceanogr.*, 36, 592–605.

Johnson, G. C., B. M. Sloyan, W. S. Kessler, and K. E. McTaggart (2002), Direct measurements of upper ocean currents and water properties across the tropical Pacific during the 1990s, *Prog. Oceanogr.*, 52, 31–61.

Kalnay, E., et al. (1996), The NCEP/NCAR 40-year reanalysis project, *Bull. Am. Meteorol. Soc.*, 77, 437–471.

Katz, E. J., R. L. Molinari, D. E. Cartwright, P. Hisard, H. U. Lass, and A. deMesquita (1981), The seasonal transport of the Equatorial Undercurrent in the western Atlantic (during the Global Weather Experiment), *Oceanol. Acta*, 4(4), 445–450.

Keenlyside, N., and R. Kleeman (2002), Annual cycle of equatorial zonal currents in the Pacific, *J. Geophys. Res.*, 107(C8), 3093, doi:10.1029/2000JC000711.

Keenlyside, N. S., and M. Latif (2007), Understanding Equatorial Atlantic interannual variability, *J. Clim.*, 20(1), 131–142.

Kleeman, R., J. P. McCreary, and B. A. Klinger (1999), A mechanism for generating ENSO decadal variability, *Geophys. Res. Lett.*, 26(12), 1743–1746.

Kraus, E. B., and J. S. Turner (1967), A one-dimensional model of the seasonal thermocline: I. A laboratory experiment and its interpretation, *Tellus*, 19, 88–97.

Kushnir, Y., W. A. Robinson, P. Chang, and A. W. Robertson (2006), The physical basis for predicting Atlantic sector seasonal-to-interannual climate variability, *J. Clim.*, 19, 5949–5970.

Liu, Z., S. G. H. Philander, and R. C. Pacanowski (1994), A GCM study of tropical-subtropical upper-ocean water exchange, *J. Phys. Oceanogr.*, 24, 2606–2623.

Lumpkin, R., and S. L. Garzoli (2005), Near-surface circulation in the tropical Atlantic Ocean, Part II: Time-mean currents and seasonal variability, *Deep Sea Res., Part I*, 52(3), 495–518.

Lumpkin, R., and K. Speer (2003), Large-scale vertical and horizontal circulation in the North Atlantic Ocean, *J. Phys. Oceanogr.*, 33, 1902–1920.

Malanotte-Rizzoli, P., K. Hedstrom, H. Arango, and D. B. Haidvogel (2000), Water mass pathways between the subtropical and tropical ocean in a climatological simulation of the North Atlantic Ocean circulation, *Dyn. Atmos. Oceans*, 32, 331–371.

McCreary, J. P., and P. Lu (1994), Interaction between the subtropical and equatorial ocean circulations: The subtropical cell, *J. Phys. Oceanogr.*, 24, 466–497.

Mercier, H., M. Arhan, and J. R. E. Lutjeharms (2003), Upper-layer circulation in the eastern Equatorial and South Atlantic Ocean in January-March 1995, *Deep Sea Res., Part I*, 50, 863–887.

Merle, J. (1980), Variabilité thermique annuelle et interannuelle de l'océan Atlantique équatorial Est. L'hypothèse d'un "El Niño" Atlantique, *Oceanol. Acta*, 3, 209–220.

Moore, D., and S. Philander (1976), Modelling of the tropical oceanic circulation, in *The Sea*, vol. 6, pp. 319–361, John Wiley, Hoboken, N. J.

Pacanowski, R. C. (1995), MOM 2-documentation, User's Guide and Reference Manual, *Tech. rep.*, Geophysical Fluid Dynamics Laboratory, Princeton, NJ, USA.

Pacanowski, R. C., and S. G. H. Philander (1981), Parameterization of vertical mixing in numerical models of tropical oceans, *J. Phys. Oceanogr.*, 11, 1443–1451.

Peter, A.-C., M. L. Hénaff, Y. du Penhoat, C. E. Menkes, F. Marin, J. Vialard, G. Caniaux, and A. Lazar (2006), A model study of the seasonal mixed layer heat budget in the equatorial Atlantic, *J. Geophys. Res.*, 111, C06014, doi:10.1029/2005JC003157.

Peterson, R. G., and L. Stramma (1991), Upper-level circulation in the South Atlantic Ocean, *Prog. Oceanogr.*, 26, 1–73.

Philander, S. G. H., and R. C. Pacanowski (1980), The generation of equatorial currents, *J. Geophys. Res.*, 85, 1123–1136.

Philander, S. G. H., and R. C. Pacanowski (1986a), A model of the seasonal cycle in the tropical Atlantic Ocean, *J. Geophys. Res.*, 91, 14,192–14,206.

Philander, S. G. H., and R. C. Pacanowski (1986b), The mass and heat budget in a model of the tropical Atlantic Ocean, *J. Geophys. Res.*, 91, 14,212–14,220.

Philander, S. G. H., W. J. Hurlin, and A. D. Seigel (1987), Simulation of the seasonal cycle of the tropical Pacific Ocean, *J. Phys. Oceanogr.*, 17, 1986–2002.

Provost, C., S. Arnault, N. Chouaib, A. Kartavtseff, L. Bunge, and E. Sultan (2004), TOPEX/Poseidon and Jason equatorial sea surface slope anomaly in the Atlantic in 2002: Comparison with winds and current measurements at 23W, *Mar. Geod.*, 27, 31–45.

Rapp, R. H., Y. Yi, and Y. Wang (1994), Mean sea surface and geoid gradient comparisons with TOPEX altimeter data, *J. Geophys. Res.*, 99(C12), 24,657–24,668.

Redler, R., K. Ketelsen, J. Dengg, and C. Böning (1998), *A high-resolution model for the circulation of the Atlantic Ocean*, fourth European SGI/CRAY MPP Workshop, Garching.

Reynolds, R. W., and T. M. Smith (1994), Improved global sea surface temperature analysis using optimum interpolation, *J. Clim.*, 7, 929–948.

Reynolds, R. W., N. A. Rayner, T. M. Smith, D. C. Stokes, and W. Wang (2002), An improved in situ and satellite SST analysis for climate, *J. Clim.*, 15, 1609–1625.

Ruiz-Barradas, A., J. A. Carton, and S. Nigam (2000), Structure of interannual-to-decadal climate variability in the tropical Atlantic sector, *J. Clim.*, 13, 3285–3297.

Schott, F. A., and C. W. Böning (1991), The WOCE model in the western Equatorial Atlantic: Upper layer circulation, *J. Geophys. Res.*, 96(C4), 6993–7004.

Schott, F. A., P. Brandt, M. Hamann, J. Fischer, and L. Stramma (2002), On the boundary flow off Brazil at 5–10°S and its connection to the interior tropical Atlantic, *Geophys. Res. Lett.*, 29(17), 1840, doi:10.1029/2002GL014786.

Schott, F. A., M. Dengler, P. Brandt, K. Affler, J. Fischer, B. Bourlès, Y. Gouriou, R. L. Molinari, and M. Rhein (2003), The zonal currents and transports at 35°W in the tropical Atlantic, *Geophys. Res. Lett.*, 30(7), 1349, doi:10.1029/2002GL016849.

Schott, F. A., J. P. McCreary, and G. C. Johnson (2004), Shallow Overturning Circulations of the Tropical-Subtropical Oceans, in *Earth's Climate: The Ocean-Atmosphere Interaction and Climate Variability*, edited by C. Wang, S.-P. Xie, and J. A. Carton, Geophysical Monograph Series 147, AGU, Washington, D. C.

Servain, J., J. Picaut, and J. Merle (1982), Evidence of remote forcing in the equatorial Atlantic Ocean, *J. Phys. Oceanogr.*, 12, 457–463.

Snowden, D. P., and R. L. Molinari (2003), Subtropical Cells in the Atlantic Ocean: An Observational Summary, in *Interhemispheric Water Exchange in the Atlantic Ocean*, edited by G. J. Goni and P. Malanotte-Rizzoli, pp. 287–312, Elsevier Oceanographic Series.

Verstraete, J.-M. (1992), The seasonal upwellings in the Gulf of Guinea, *Prog. Oceanogr.*, 29, 1–60.

Wacongne, S. (1989), Dynamical regimes of a fully nonlinear stratified model of the Atlantic Equatorial Undercurrent, *J. Geophys. Res.*, 94, 4801–4815.

Weisberg, R. H., J. H. Hickman, T. Y. Tang, and T. J. Weingartner (1987), Velocity and temperature observations during the seasonal response of the equatorial Atlantic experiment at 0°, 28°W, *J. Geophys. Res.*, 92(C5), 5061–5075.

Willebrand, J., et al. (2001), Circulation characteristics in three eddy-permitting models of the North Atlantic, *Prog. Oceanogr.*, 48, 123–161.

Xie, S.-P., and J. A. Carton (2004), Tropical Atlantic Variability: Patterns, Mechanisms, and Impacts, in *Earth's Climate: The Ocean-Atmosphere Interaction and Climate Variability*, edited by C. Wang, S.-P. Xie and J. A. Carton, Geophysical Monograph Series 147, AGU, Washington, D. C.

Yu, X. R., and M. J. McPhaden (1999), Dynamical analysis of seasonal and interannual variability in the equatorial Pacific, *J. Phys. Oceanogr.*, 29(9), 2350–2369.

Yu, L., X. Jin, and R. A. Weller (2006), Role of net surface heat flux in seasonal variations of sea surface temperature in the tropical Atlantic Ocean, *J. Clim.*, 19, 6153–6169.

Zebiak, S. E. (1993), Air-sea interaction in the equatorial Atlantic region, *J. Clim.*, 6, 1567–1586.

Zhang, D., M. J. McPhaden, and W. E. Johns (2003), Observational evidence for flow between the subtropical and tropical Atlantic: The Atlantic subtropical cells, *J. Phys. Oceanogr.*, 33(8), 1783–1797.

────────────────

P. Brandt and V. Hormann, Leibniz-Institut für Meereswissenschaften an der Universität Kiel, Düsternbrooker Weg 20, 24105 Kiel, Germany. (vhormann@ifm-geomar.de)